Journal of
Composites Science

MDPI

Article

Numerical Study on the Performance and Failure Modes of Bolted Connections in Pultruded-Fibre-Reinforced Polymer (PFRP) Profiles

Abdur Rahman *, Ingrid Boem * and Natalino Gattesco

Department of Engineering and Architecture, University of Trieste, 34127 Trieste, Italy; gattesco@units.it
* Correspondence: abdur.rahman@phd.units.it (A.R.); ingrid.boem@dia.units.it (I.B.)

Abstract

The use of pultruded-fibre-reinforced polymer (PFRP) composite profiles in structural applications is rapidly increasing, due to their high strength-to-weight ratio, corrosion resistance, and durability. Bolted joints between PFRP play a critical role, as localized high stresses in a material that typically exhibits brittle behaviour—especially in tension and shear—can lead to sudden failure. This study aims to investigate the mechanical performance of such bolted connections (in terms of stiffness, strength, displacement capacities and failure modes), contributing to the development of reliable yet optimized design criteria for structural applications. In particular, numerical analyses of single-bolted connections in PFRP profiles are presented in the paper. To emphasize the general validity of the model and demonstrate its applicability across different configurations, the simulations were validated against experimental results from three separate test campaigns, which varied in both material (three different PFRP composites) and geometry (profile thickness, bolt diameter, and hole–end distance). Finite element models using continuum shell elements in ABAQUS, based on the Hashin failure criteria, successfully captured typical failure modes, including shear-out and pin-bearing. Two analysis approaches—implicit and explicit solvers—were also compared and discussed. Sensitivity analyses were carried out to enhance the model's accuracy and its computational efficiency. The validated model was then extended to simulate different configurations, investigating the role of the main parameters influencing the connections.

Keywords: composite profiles; bolted connections; numerical simulations; explicit solver; implicit solver

check for updates

Academic Editors: Haifeng Zhao, Konstantinos Tserpes, Salim Belouettar and Marcin Kamiński

Received: 30 July 2025
Revised: 1 September 2025
Accepted: 6 September 2025
Published: 10 September 2025

Citation: Rahman, A.; Boem, I.; Gattesco, N. Numerical Study on the Performance and Failure Modes of Bolted Connections in Pultruded -Fibre-Reinforced Polymer (PFRP) Profiles. *J. Compos. Sci.* **2025**, *9*, 492. https://doi.org/10.3390/jcs9090492

1. Introduction

Fibre-reinforced polymers (FRPs) are composite materials composed of high-strength fibres embedded within a polymer matrix [1–4]. The fibres impart strength and stiffness to the composite, while the matrix binds the fibres together, enabling them to act as a unified material system and protect them from environmental damage. The reinforcing fibres are typically synthetic, such as carbon, glass, aramid, or basalt fibres, although natural cellulose-based fibres (e.g., jute, hemp) are also increasingly utilized for developing sustainable composites. The polymer matrix is generally a thermoset resin, such as epoxy, polyester, or vinyl ester. By varying the type and proportion of fibres and polymer matrix, a wide range of composite materials with tailored mechanical properties can be produced. These composites are manufactured through various processes, including weaving, hand lay-up, resin transfer moulding, vacuum bagging, and pultrusion. Pultrusion is particularly common for producing continuous composite profiles; in this process, fibres are drawn through a resin bath and subsequently cured as they are pulled through a heated die.

The use of pultruded-fibre-reinforced polymer (PFRP) composite profiles in civil engineering has grown rapidly over the past three decades in civil engineering [1–7]. Initially, their application was limited to the repair, strengthening, and retrofitting of concrete and masonry structures [8–13]. However, in recent years, their adoption has expanded significantly due to their versatile properties, such as their light weight combined with their high strength and stiffness, their resistance to corrosion, their controllable thermal properties, their lower life cycle cost, their enhanced fatigue life and the fact that they are inert towards magnetics [5]. These characteristics make composite profiles highly advantageous for a variety of structural applications. Glass-fibre-reinforced polymer (GFRP) profiles are most commonly used in construction of new infrastructures like pedestrian bridges, communication towers and low-rise buildings.

PFRP profiles can be assembled using various methods, including bolted connections, adhesive joints, or a combination of both. Among these, bolted connections are the most commonly used in civil engineering structures. The preference for bolted connections is primarily due to their ease of construction, faster assembly, and straightforward disassembly for inspection and maintenance purposes, and they are also the most economical and cost-effective [14–16]. However, a critical aspect of using PFRP profiles is the connection itself, as it is often the point where stress concentration occurs. Proper design and analysis of these connections are thus crucial to ensure the structural integrity and performance of the system.

Bolted connections in PFRP profiles can fail in several modes, depending on various factors such as the composition of the material (i.e., fibres amount and orientation), the geometry of the jointed profiles, the position of the bolts and the loading direction. The primary failure modes include pin-bearing, shear-out, cleavage, splitting and net tension, as shown in Figure 1. Extensive research and experimental campaigns have been conducted to understand the conditions under which these failures occur [7,14,15,17–22].

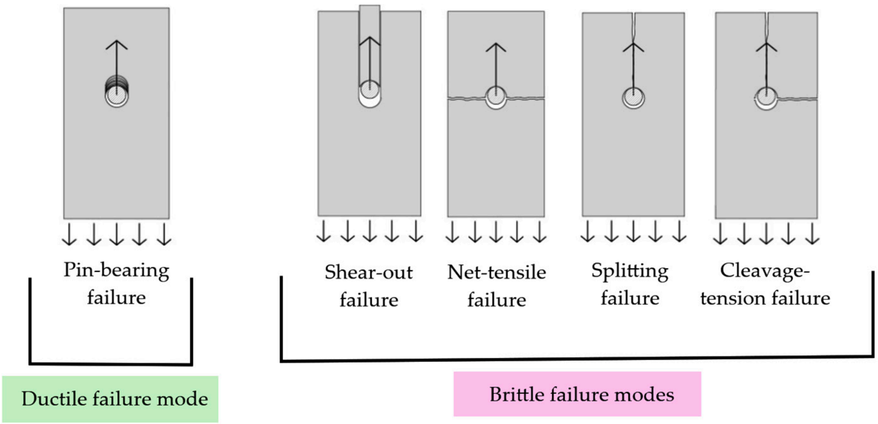

Figure 1. Schematization of typical failure modes of GFRP bolted connections subjected to longitudinal tensile load.

For example, referring to load along the longitudinal pultrusion direction, Rosner and Rizkalla and [14] carried out a comprehensive experimental programme to investigate the effects of geometric parameters, such as end distance (e) and plate width (w), with respect to bolt diameter (d), on the performance of GFRP bolted connections. Single-bolted, double-lap joints were studied: when e/d = 1–3 and $w/d \geq 5$, the dominant failure mode was cleavage failure (i.e., an initial crack parallel to the applied loading direction developed at the end of the plate along the end distance and started growing towards the plate hole, thereby leading to the development of other fractures and cracks around the net section due to formation of in-plane bending stresses). When $w/d < 5$, net tension failure occurred, regardless e/d (e/d = 1–12); it was characterized by a crack along the net section perpendicular to the applied load. As e/d and w/d both increased to ≥ 5, the failure shifted towards more favourable bearing failure (i.e., localized crushing of the material in the vicinity of the bolt hole, with an enlargement of the plate hole). They further observed that the connection resistance increased approximately linearly with increasing plate thickness (t = 9.5 to 19.1 mm).

Abd-El-Naby et al. [19] carried out an experimental campaign on double-lap joints using two different types of GFRP materials, namely grey (52 specimens) and yellow (45 specimens). The grey material consisted of 73% unidirectional fibres and 27% outer layers of chopped strand mat (CSM), whereas the yellow material contained 59% unidirectional rovings and a higher proportion of CSM (41%). The bolt diameter was fixed at 9.5 mm. For the grey material, e varied from 40 to 140 mm and w between 30 and 70 mm; for the yellow one, e = 30 to 70 mm and w = 20 to 38 mm. The experimental results revealed three primary failure modes: net tension, shear-out, and bearing. For the yellow material, net tension failure within the CSM layers occurred when the specimens had a small w combined with a large e. Shear-out failure in the central unidirectional fibre layer, characterized by the formation of a hat-shaped wedge, was observed when e was small. When both the e and w were increased, bearing failure occurred in the outer CSM layers, while shear-out failure developed in the central unidirectional fibre layers. For the grey material, w was sufficiently large and only shear-out and bearing failures occurred. When there was a small e, the shear-out failure was abrupt; when there was an intermediate e, it became gradual; for a large e, bearing failure occurred. The critical end distance was defined, for each w, as the distance at which the maximum resistance of the connection was attained, beyond which further increases in the end distance did not enhance strength. The increased thickness of CSM in the yellow material enabled a more uniform distribution of stresses compared to the grey material.

Tajeuana et al. [21] conducted an experimental study on single-bolt GFRP joints, focusing primarily on single-lap configurations to assess the effects of varying end distances and side distances (s), with respect to bolt diameter. In single-lap joints with e/d = 3 and s/d = 2, cleavage failure was predominant. Occasionally, shear-out and net tension failures also occurred. Increasing both e/d and s/d to 4 definitely shifted the failure mode to shear-out and improved the peak load capacity. A few double-lap joints with e/d = 3 and s/d = 2 were also tested, showing cleavage failure. Double-lap joints exhibited a more stable load–displacement response and higher load capacity than single-lap joints, due to their symmetrical loading, which minimized out-of-plane bending and other secondary effects.

Martin et al. [17] performed experimental tests on double-lap joints with various end distances (e/d = 1.9, 3.1, 4.4, and 8.8) while keeping w/d = 5. They observed that for the specimens with the two lower e/d ratios, sudden shear-out failure occurred, with an abrupt loss of resistance after the peak. For the highest e/d ratio, the failure mode was pin-bearing and the load was also almost maintained under a large displacement, when shear-out failure was also observed. For an intermediate e/d ratio, localized pin-bearing failure was initially observed, but it was immediately followed by shear-out failure.

The effect of loading direction has been extensively investigated by several researchers, who have addressed inclined and transverse loading conditions with respect to the main pultrusion direction. For example, Rosner and Rizkalla [14] compared longitudinal (0°), inclined (45°) and transverse (90°) loading conditions, varying the e/d and w/d ratios. Net tension failure occurred for both inclined (45°) and transverse (90°) loading, for configurations with e/d and w/d ratios ranging from 1 up to higher values of 10. When the

w/d ratio was further increased (13.4), cleavage failure occurred at $e/d = 1$, and this then shifted to net tension failure for e/d = 2–5. For $e/d = 10.7$, pin-bearing failure occurred. The cleavage failure that typically occurred under longitudinal (0°) loading was suppressed under inclined (45°) and transverse (90°) loading when $w/d \geq 5$ and $e/d < 4$. Cleavage and bearing failure required larger widths ($w/d \geq 13$) to avoid net tension failure. Overall, it was observed that the resistance of the connection under longitudinal loading (0° along the main pultrusion direction) was 18% and 24% higher than that under the inclined (45°) and transverse (90°) loading directions, respectively.

Turvey [18] analyzed single-bolt connections under longitudinal (0°), transverse (90°), and inclined (30° and 45°) loading. Four different width-to-diameter ratios (w/d = 4, 6, 8, and 10) were considered. Under the transverse loading condition, the ultimate resistance increased with increasing w/d ratios; however, net tension remained as the failure mode. For the longitudinal loading direction, the failure mode was dependent on the e/d ratio: when $e/d \geq 4$, bearing failure occurred, whereas for $e/d < 4$, shear-out failure was observed. In the case of inclined loading condition (30° and 45°), net tension failure occurred consistently, even for larger e/d ratios of 6 and w/d ratios of 10, highlighting the dominance of transverse tensile stresses in these orientations.

In general, referring to the main loading direction (i.e., the longitudinal one), shear-out failure tends to dominate when the end distance of the connection is small. On the other hand, net tension failure is more likely to occur when the width of the profile is insufficient. If both the end distance and width are inadequate, cleavage failure can result. Conversely, when both the end distance and width are sufficient, bearing failure typically occurs, while in the transverse and inclined loading conditions, net tension failure is more likely to dominate due to the lower transversal tensile strength. Among these failure modes, bearing failure is the most desirable, because it is ductile in nature, allowing for large deformations and providing warnings before final failure, also enabling load distribution in the case of multi-bolt connections. In contrast, shear-out, net tension, cleavage and splitting failures are brittle, leading to sudden and catastrophic failure without any prior indication.

Unlike steel, for which standardized guidelines and well-defined testing procedures are firmly established, FRPs present a significant challenge for universal standardization due to their inherently variable compositions. The mechanical properties of composites are highly sensitive to the type, volume fraction, and orientation of fibres, as well as to the nature of the polymer matrix. As a result, even minor changes in constituent materials or manufacturing processes can lead to substantial variations in structural behaviour. To provide a framework for design, several standards and guidelines have been developed. These include EN 13706 [23], which specifies requirements and test methods for pultruded profiles in structural applications, the EUROCOMP Design Code and Handbook [24], which offers comprehensive design recommendations and classification systems, and CNR-DT 205/2007 [25], an Italian guide that details the design and execution of structures using PFRP elements.

Despite these established documents, the inherent variability of composite materials means that experimental characterization remains indispensable whenever the composition or fibre architecture changes. Testing is essential to accurately determine mechanical and strength properties in the longitudinal, transverse and out-of-plane directions. Moreover, conducting exhaustive experimental campaigns to capture the strength and failure modes of composite connections is essential. But experimental testing is often complex and time-consuming, particularly given the vast array of possible geometric configurations and loading conditions. To address this, researchers have increasingly turned to numerical simulations, leading to the development of a variety of failure criteria to predict damage initiation and evolution in composite structures. FRP-specific material models are required, rather than directly the isotropic models commonly used in civil engineering (e.g., for steel or concrete), since FRP composites are strongly anisotropic/orthotropic, with properties that vary by direction, and they fail through multiple distinct modes in the longitudinal and transverse directions (fibre tension, fibre compression, matrix tension, and matrix compression). Consequently, accurate prediction of the damage initiation and progression of these failure modes requires anisotropic constitutive laws and mechanism-specific failure criteria combined with progressive-damage formulations. Among these, the Hashin [26], Puck [27], and Larc05 [28] failure criteria are widely recognized and extensively used. These failure criteria assess damage in both fibres and the matrix under different loading conditions. Moreover, in recent years, progressive-damage models have been employed to track damage evolution under loading. ABAQUS [29] includes an in-built Hashin failure criterion; however, its applicability is limited to shell and continuum shell elements. More recently, the Larc05 criterion has also been integrated into ABAQUS versions 2024 and 2025 for shell and continuum shell elements.

Numerical modelling of FRP-bolted joints is carried out mostly in the aircraft industry but also in civil engineering, and it has been widely explored to reduce the need for extensive and often costly experimental campaigns [21,30–47]. Over time, these models have evolved significantly, ranging from simplified two-dimensional (2D) analyses to more detailed three-dimensional (3D) representations, and from purely linear elastic formulations to advanced progressive-damage models capable of capturing nonlinear and failure behaviours.

Among these, Turvey and Wang [31] developed 2D (FE) models by using ANSYS FE software [48] for single-bolt tension joints in pultruded GFRP plates, accounting for factors such as bolt–hole clearance and friction. Their study highlighted the inadequacy of simplified normalized stress-based design approaches, such as those adopted in the EUROCOMP code [24], due to the sensitivity of stress distributions to contact conditions and applied loads. However, their model remained within the elastic regime and did not incorporate damage progression or post-elastic behaviour. To address this limitation, various researchers have developed two- and three-dimensional progressive-damage models, enabling accurate damage assessment in the nonlinear range.

Tajeuna et al. [21] developed a two-dimensional finite element model using ADINA 8.7.3 [49] to simulate single-bolt, single-lap and double-lap GFRP–steel connections to investigate the influence of geometric parameters. The GFRP plate was discretized with nine-node quadrilateral elements, using a refined mesh around the bolt hole to improve accuracy. The material behaviour was modelled as orthotropic plasticity, with input parameters derived from experimentally measured tensile properties, including ultimate strain. The bolt was idealized as a rigid half-cylinder to reduce computational cost, and contact between the bolt and plate was defined using ADINA's surface contact formulation. The model was first validated against experimental results for both joint types, showing good agreement in peak strength and failure modes. A parametric study was then conducted varying both the end distance and side distance in the ranges of $1 \leq e/d \leq 5$ and $1 \leq s/d \leq 5$. While the numerical model successfully captured all observed failure modes, the load–displacement response beyond the peak load was not simulated. This limitation may be attributed to convergence difficulties or the intrinsic restrictions of the analysis setup.

Du et al. [50] developed a three-dimensional progressive-damage model in Abaqus/Explicit to simulate the behaviour of double-lap joints in pultruded GFRP composites. Their approach integrated a nonlinear shear response, the Hashin failure criteria, and a strain-based continuous stiffness degradation law into an explicit vectorized custom-defined user material (VUMAT) subroutine. This allowed the model to capture the progressive damage evolution of the composite under quasi-static loading, which was applied using a gradually increasing displacement. The numerical predictions showed good agreement with the experimental results, validating the effectiveness of the model. However, a key limitation of this approach is that the progressive-damage formulation is not natively available in ABAQUS. It requires users to compile and integrate the VUMAT subroutine with ABAQUS, which can be technically demanding and presents a significant barrier for many structural engineers without advanced programming or finite element backgrounds.

Recently, Arruda et al. [43] introduced an implicit three-dimensional damage model based on the Hashin failure criterion. This user-defined material (UMAT) model customizes damage initiation and progression by incorporating fracture energies and residual strength parameters in a user subroutine in the implicit solver. To mitigate convergence issues, the model employs an implicit-to-explicit solver. The shear-out and pin-bearing failure were simulated without having any convergence problems.

Liu et al. [45] developed a numerical model for a single-lap joint between a carbon–FRP laminate and a steel plate using countersunk fasteners. In their approach, continuum shell elements were used to capture intralaminar ply failure, while cohesive elements were implemented to simulate interlaminar damage under Mode I (traction) loading. For Mode II (shear) and mixed-mode delamination, a user-defined VUMAT incorporating 3D Hashin failure criteria and the Camanho degradation law [51] was employed. Their simulations, performed using the ABAQUS/Explicit solver [29], showed excellent agreement with the experimental results, and no convergence issues were reported. However, their study was limited to modelling bearing failure as the dominant failure mode.

To the best of the authors’ knowledge, the application of ABAQUS/Explicit using in-built failure criteria has not yet been explored in detail for FRP-bolted joints. While several 2D and 3D user-defined material models are available in the literature [43,50] for PFRP composites, they are not directly accessible within ABAQUS. These models often require significant computational effort, specialized expertise, and additional software integration for pre- and post-processing, which limits their practical usability. This paper aims to address this gap by employing the built-in composite damage modelling capabilities of ABAQUS/Explicit to simulate the response of FRP-bolted joints. The main purpose is to evaluate the capability and reliability of the developed model in simulating the performance of bolted joints—including the prediction of the different failure modes and the post-elastic behaviour—and to thoroughly understand the role of the different fundamental mechanical parameters that govern the performance. Different GFRP materials and joint configurations are considered to achieve more thorough and robust validation.

In this manuscript, the general features of the numerical model for single-bolted joints are first presented. This is followed by a description of the three types of composite materials considered for validation, and the corresponding experimental features and results obtained for double-lap connections. The reliability of the numerical model is then proven by comparison with the experimental data for all material types and configurations. Furthermore, comprehensive sensitivity analysis is conducted to optimize computational efficiency while maintaining acceptable accuracy. In addition, parametric analyses are performed to evaluate the influence of the main material’s mechanical properties on the performance of the connection.

2. Numerical Model Features

The numerical model of the single-bolted double-lap joint shown in Figure 2a was developed in the latest version of ABAQUS/Explicit version 2025 [29]. The general configuration consists of two steel plates with an inner GFRP pultruded plate. The X-axis was designated as the longitudinal direction of the GFRP plate, aligned with the unidirectional roving, which corresponds to the direction of the major elastic modulus. To reduce computational costs, only one-fourth of the model was developed, with symmetry boundary conditions applied in both the Y and Z directions. The steel plate was modelled with the full length and thickness but half the width, while the composite plate was modelled with the full length, half the thickness, and half the width. Additionally, one-fourth of the bolt was modelled. The far end of the GFRP composite plate was fully constrained in all directions, and a linearly increasing X displacement was applied to the far end of the steel plate to replicate the experimental loading conditions. A 1 mm gap was maintained between the plates, consistent with the experimental setups.

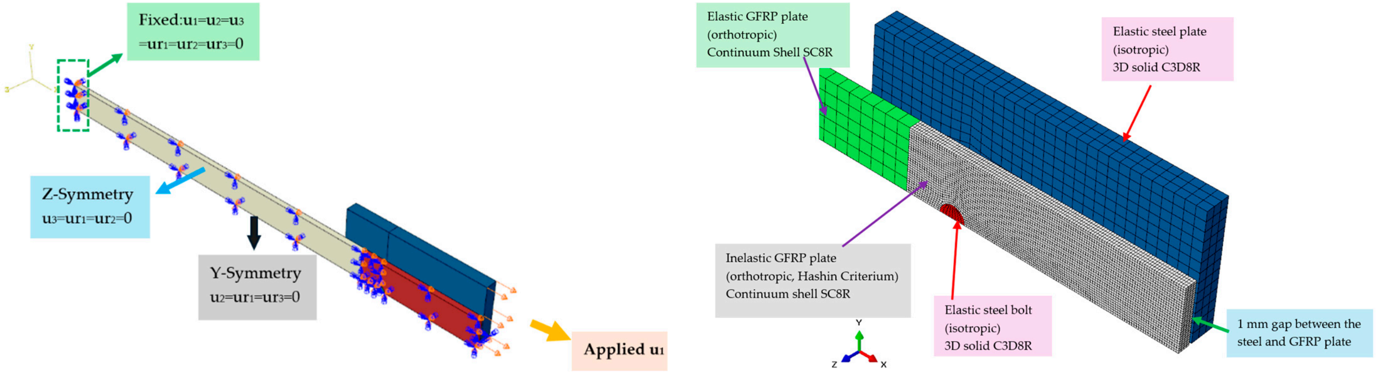

(**a**) (**b**)

Figure 2. A generalized model description for single-bolted, double-lap joints in ABAQUS: (**a**) boundary conditions and (**b**) partial description with meshing.

The continuum shell elements with eight nodes and reduced integration (SC8R) were selected for the composite plate, which was modelled in two separate parts, one being assigned only elastic properties, and the other—surrounding the bolt region, where stress concentrations and failures are expected—being assigned mechanical failure-capable properties (nonlinear behaviour). The elastic and inelastic parts of GFRP plates were tied together. Orthotropic engineering constants were considered for both. Additionally, the built-in Hashin damage failure and progression criteria (applicable only for shell and continuum shell elements) were assigned to the inelastic part. The inelastic plate was assigned tensile, compressive, and shear strength parameters in both the longitudinal and transverse directions for damage initiation. For damage progression, the tensile and compressive fracture energies were specified in the longitudinal and transverse directions. The details of these parameters are explained later in Section 4. On the other hand, continuum three-dimensional solid elements with reduced integration (C3D8R) and with isotropic elastic behaviour were used for both the bolt and steel plate. The combination of SC8R and C3D8R elements ensured both an accurate representation of composite damage mechanisms in the FRP and a reliable simulation of the steel components. The general contact algorithm for the explicit solver was applied for the contact between the bolt and the steel plate and also between the bolt the GFRP plate. Contact interactions between the plate and bolt were defined as hard contact in the normal direction, and a coefficient of friction of 0.2 was applied in the tangential direction, as recommended by various researchers [31,43].

The mesh size for the steel plate was set to $3 \times 3 \times 3$ mm^3, while the bolt was meshed at $1 \times 1 \times 1$ mm^3. For the elastic region of the composite plate, we used a mesh size of $4 \times 4 \times 4$ mm^3, and the region around the bolt was refined to $0.7 \times 0.7 \times 1$ mm^3, with 1 mm in the thickness direction. A mesh sensitivity analysis was performed (as detailed in Section 5.3 of the manuscript), and the mesh size was selected as the ideal compromise between accuracy and computational efficiency. The explicit solver with a dynamic procedure was used to perform the simulations. The displacement applied on the steel plate was increased gradually, to avoid dynamic effects, ensuring that the kinetic energy remained negligible throughout the simulation, with respect to the input energy. Mass scaling with a target increment of 5×10^{-7} was set to reduce the computational time without compromising the accuracy of the analysis (the duration of the simulation on a machine with 8 CPUs was reduced approximately from 24 to 42 h to 2–6 h). However, preliminary sensitivity analyses were performed to compare the capabilities of the explicit solver with those of the implicit one and to properly calibrate the mass scaling and mesh size, as will be discussed later in Section 5.

3. Experimental References

Three different experimental campaigns were selected to carry out the numerical simulations of single-bolted double-lap joints, considering different GFRP materials. This selection was based on the need to cover various composite GFRP materials and various geometric configurations. The mechanical characteristics for the three GFRP materials denoted as Type-A, Type-B and Type-C are shown in Table 1 and are described in the subsequent sub-sections.

Table 1. Mechanical properties of GFRP pultruded profiles.

Property	**Type-A**	**Type-B**	**Type-C**	**Standards for Type-A**	**Standards for Type-B and Type-C**
Longitudinal Tensile Strength (MPa)	334	395	360	EN ISO 527-1 [52]	EN ISO 527-1
Longitudinal Compressive Strength (MPa)	316	440	280	ASTM-D695 [53]	EN ISO 14126 [54]
Transverse Tensile Strength (MPa)	29	19	100	--- [43]	EN ISO 527-1
Transverse Compressive Strength (MPa)	51.9	45	35	ASTM-D695	EN ISO 14126
In-plane Shear Strength (MPa)	35	19	50	ASTM-D5379 [55]	EN ISO 14130 [56]
Longitudinal Young's Modulus (MPa)	23,100	32,600	27,000	ASTM-D695	EN ISO 527-4
Transverse Young's Modulus (MPa)	2900	3800	7000	ASTM-D695	EN ISO 527-4
In-plane Shear Modulus (MPa)	3000	3029	5800	ASTM-D5379	EN ISO 14130
Interlaminar shear modulus (MPa)	2500	2500	5800	ASTM-D2344 [57]	--- [58,59]
Interlaminar shear strength (MPa)	33.8	19	30	ASTM-D2344	--- [58,59]
Poisson ratio (υ_{12})	0.28	0.23	0.23	EN ISO 527-1 [52]	EN ISO 527-1 [52]
Poisson ratio (υ_{23})	0.3	0.28	0.28	--- [43]	--- [58,59]

For the mechanical parameters not determined experimentally (---), values from the literature were assumed.

3.1. GFRP Material "Type-A"

Martin et al. [17] carried out a broad experimental testing campaign on single-bolted double-lap joints. The GFRP material, denoted by "Type-A" for simplicity onward in this paper, was thoroughly characterized experimentally, and the detailed properties, along with the test procedures, are reproduced in Table 1. Typical values from the literature [43] were selected when the experimental test was not applicable (transverse tensile strength and Poisson's ratio υ_{23}). The Type-A material was made from E-glass fibres and an isophthalic polyester resin matrix, in which the mass fibre ratio was 55%.

Experimental testing was performed on plates t = 8 mm thick and w = 40 mm wide, with a bolt diameter d = 8 mm. Four different bolt–end distances were investigated, e = 15, 25, 35, and 70 mm, as illustrated in Figure 3a. The setup is schematized in Figure 3b: the composite plate was sandwiched between two stainless steel plates, with a 1 mm gap between them. Capacity curves, representing the applied axial load varying with relative displacement between section A-A in the GFRP plate and section B-B in the steel (on a base length of 350 mm), were obtained for all specimens, as shown in Figure 4. The monitored displacement thus included both the local deformation of the connection and some deformation of the plates. The specimens with end distances of 15 mm and 25 mm exhibited shear-out failure, characterized by a sudden drop in the peak load (Figure 4a). In contrast, the specimen with an end distance of 70 mm (Figure 4b) showed a slight reduction in the peak load, indicating pseudo-ductile behaviour typical of pin-bearing failure, with shear-out failure then occurring at high displacements. The specimen with an end distance of 35 mm (Figure 4b) exhibited the shear-out failure mode, but attained almost the same initial peak as the 70 mm specimen, suggesting transitional behaviour from shear-out to bearing failure.

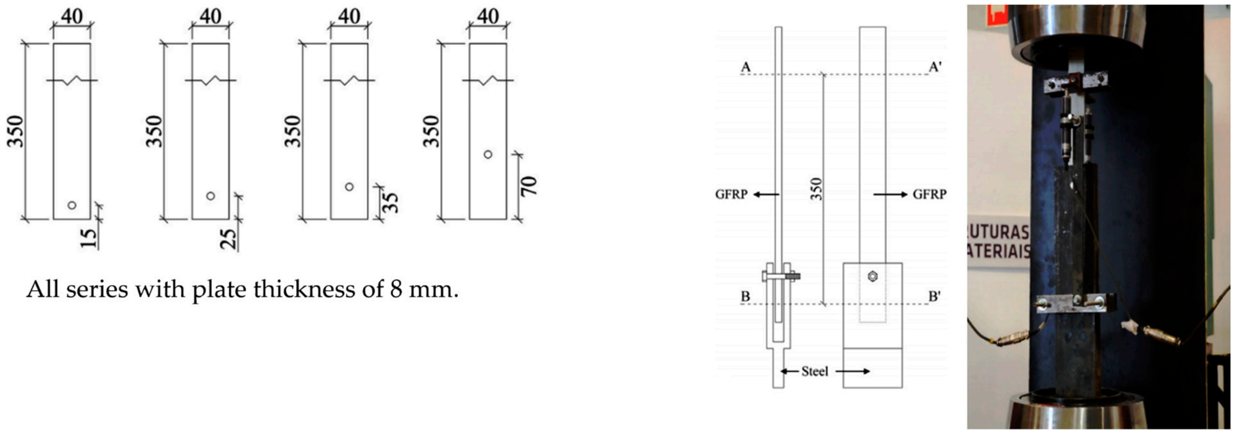

(**a**) (**b**)

Figure 3. "Type-A" based on tests on bolted connections by Martin et al. [17]: (**a**) main geometric features of the samples and (**b**) experimental setup. Reprinted with permission from Martins, D.; Gonilha, J.; Correia, J.R.; Silvestre, Thin-Walled Structures, Elsevier, 2021. © [17].

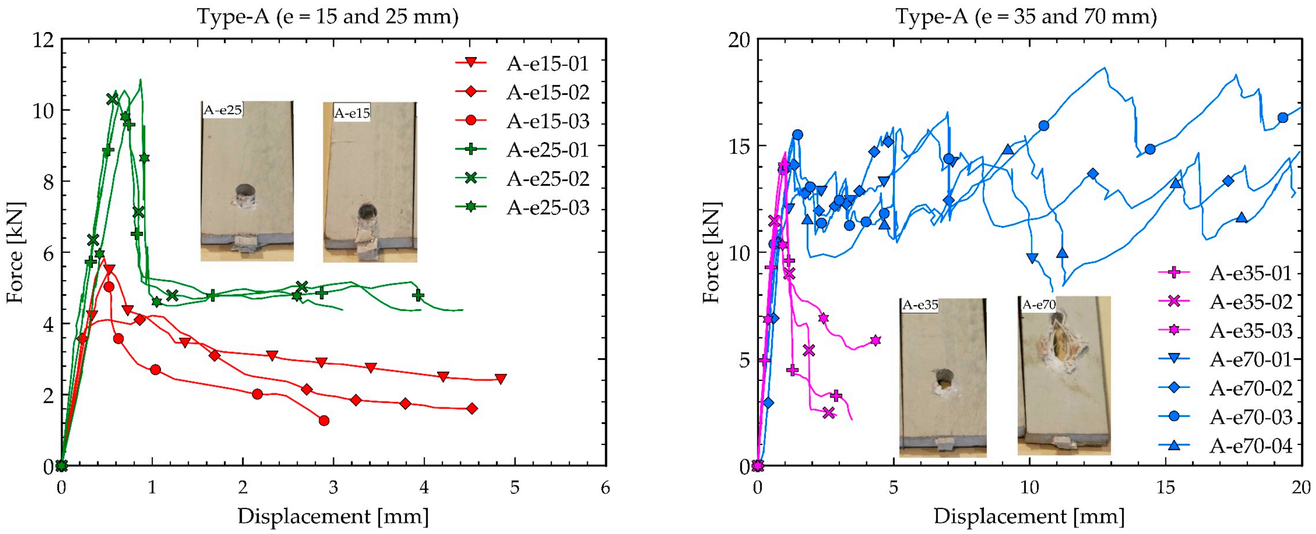

(**a**) (**b**)

Figure 4. Force vs. displacement graph for "Type-A" tests with end distances of (**a**) 15 mm and 25 mm; (**b**) 35 mm and 70 mm.

3.2. GFRP Material Type-B

Gattesco and Boem [22] considered GFRP "Type-B" plates composed of E-Glass fibre and an isophthalic polyester resin, with a fibre weight percentage of 60%. Experimental standard tests were conducted to determine the mechanical properties of the profiles according to EN ISO standards [60], and the results are summarized in Table 1. The performance of the bolted connections was evaluated on plates with dimensions of $10 \times 102 \times 300$ mm^3 and $8 \times 78 \times 230$ mm^3. A centrally located hole with diameters of 16 mm (M16) or 12 mm (M12) was created in each sample, and a close-fitting metallic pin was inserted in the hole. The bolt diameter-to-plate thickness ratio (d/t) was maintained at approximately 1.5 [24]. Additionally, the end distance-to-diameter (e/d) and width-to-diameter (w/d) ratios were kept at about six times the bolt diameter. The samples characteristics and the test setup are illustrated in Figure 5: the specimens were loaded under double shear through a rigid fork mechanism composed of three metallic plates, with 0.5 mm thick steel washers welded on the internal side of the fork brackets, acting as spacers, to prevent the lateral confinement of the GFRP plate. During the tests, the applied axial load and the relative displacement between the GFRP and the steel plates, at the height of the pin axis (i.e., the local deformation of the connection), were recorded.

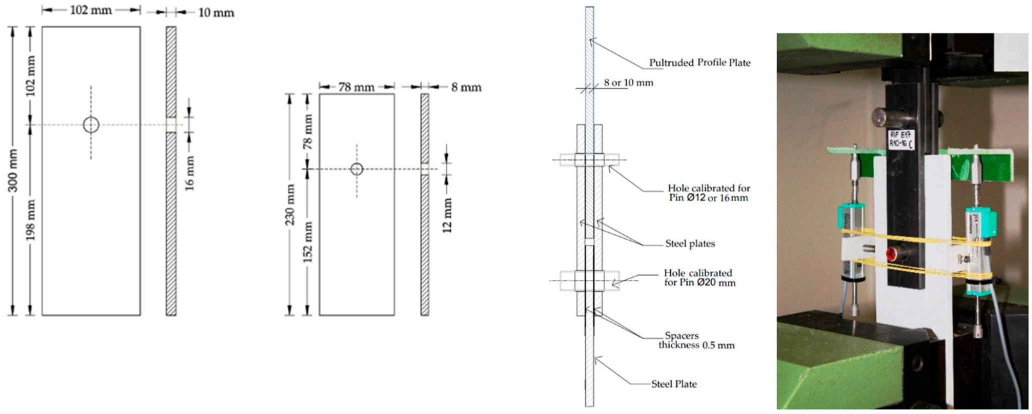

(**a**) (**b**)

Figure 5. "Type-B" based on tests on bolted connections by Gattesco and Boem [22]: (**a**) main geometric features of the samples and (**b**) experimental setup.

The force–displacement curves (Figure 6) show an initial linear elastic response, followed by local plastic deformation in the vicinity of the bolt, due to pin-bearing. A temporary drop in load occurred due to the splintering of the composite material near the bolt, after which the load increased again. Pin-bearing failure emerged, as evidenced from the evident pseudo-ductile post-peak phase. This pin-bearing failure was followed by shear-out failure at a much larger displacement in some samples, as illustrated Figure 6b. The pin-bearing load was found to be influenced by both the bolt diameter and the plate thickness. The configuration with the d = 16 mm and t = 10 mm resulted in a higher pin-bearing load compared to the configuration with a d = 12 mm bolt diameter and t = 8 mm. However, the average pin-bearing strength (evaluated as the peak load divided by $d \cdot t$) was lower in the former configuration (149.50 MPa) than in the latter (208.90 MPa).

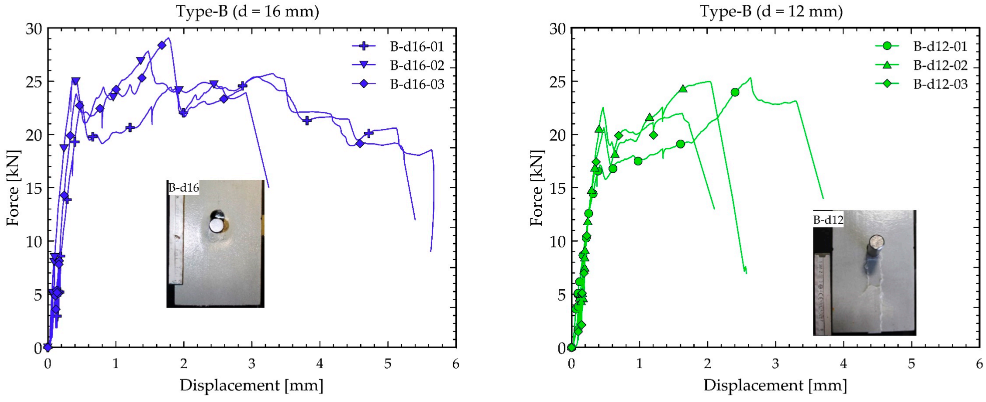

(**a**) (**b**)

Figure 6. Force–displacement graph for "Type-B" tests, with (**a**) an M16 bolt with 6d spacing, and (**b**) an M12 bolt with 6d spacing.

3.3. GFRP Material "Type-C"

The "Type-C" material was composed of E-Glass fibre and an ophthalmic polyester resin, with a fibre weight percentage of 68%; the detailed properties, which were determined from the experimental campaign, are presented in Table 1. Higher transversal and out-of-plane mechanical properties emerged with respect to Type-A and Type-B, as it also incorporates triaxial laminates layers.

Explorative tests were recently performed on single-bolt double-lap joints on GFRP plates with dimensions of 15 × 70 × 200 mm^3, as well as with a bolt hole measuring d = 13 mm and an end distance of e = 35 mm, as illustrated in Figure 7a. The test assembly consisted of an inner GFRP plate sandwiched between two outer GFRP plates with the same characteristics. The far end of the inner plate was clamped into the upper jaw of the testing machine (Figure 7b). The far ends of the outer plates were bolted to an inner steel plate measuring 10 × 50 × 200 mm^3, clamped into the lower jaw. Both connections had M12 bolts; a small torque of 18 N·m was applied, just to ensure proper alignment along the centerline. The applied load was monitored against the relative displacement between the jaws (Figure 8), thus including the deformation of the GFRP and steel plates and possible slip at the clamping heads in the measurement of the local deformation of the two connections.

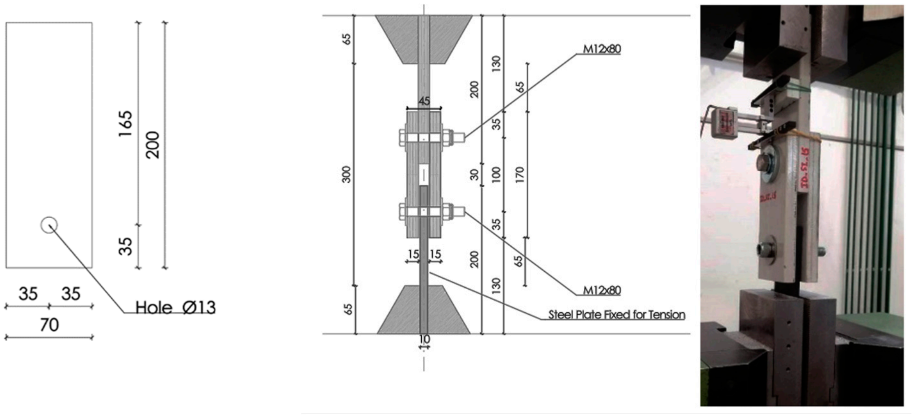

(**a**) (**b**)

Figure 7. "Type-C" tests on bolted connections: (**a**) main geometric features of the samples and (**b**) experimental setup.

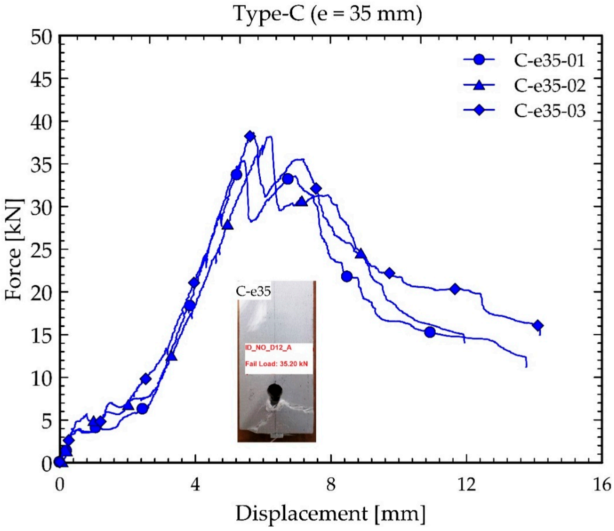

Figure 8. Force–displacement graph for "Type-C" tests, with M12 bolt and end distance of 35 mm.

After an initial elastic phase, the load–displacement curves showed a temporary but relevant stiffness reduction, from approximately 5 to 7 kN, associated with the bolts clearance recovery, once the friction between the plates, due to the small torque, was overcome. Then, the curves resumed their linear trend until the first peak was reached. Aside from this temporary effect, it was verified that the low torque did not affect the performance of the connection. The collapse of the samples was primarily dominated by the shear-out failure at the upper joint, even though with initial pin-bearing damage activation (attainment of the first peak), that immediately progressed toward the complete shear-out failure of the inner GFRP plate (second peak), as depicted in Figure 8.

4. Numerical Results

4.1. Main Parameters of the Numerical Model

The numerical model described in Section 2 was used to simulate the experimental results for the single-bolted joints collected in Section 3. The material densities were defined as 1800 kg/m^3 for the GFRP composite and 7850 kg/m^3 for the steel components. For the elastic material of the steel plates and bolts, a Young's modulus of 195 GPa and a Poisson's ratio of 0.3 were assigned for Type-A configurations and values of 210 GPa and poison ratio of 0.3 for the Type-B and Type-C configurations. For the elastic region of the GFRP plate, the orthotropic engineering constant values from Table 1 were defined in three orthogonal directions. A local coordinate system was applied to ensure the accurate representation of the material orientation, aligned with the unidirectional fibre direction.

For the inelastic region of the GFRP plate, material input included the longitudinal tensile and compressive strengths, transverse tensile and compressive strengths, and in-plane and interlaminar shear strengths from Table 1. To simulate damage progression after initiation, tensile and compression fracture energies (FEs) in both the longitudinal and transverse directions were assigned, as presented in Table 2. These values were incorporated by Arruda et al. [43] in their user-defined Hashin-based UMAT model and were obtained experimentally from a similar pultruded GFRP material by Almeida-Fernandes et al. [61]. Since the present work used the same material, the Type-A material, considered by Arruda et al. [43], along with comparable Type-B and Type-C GFRP materials, the same values were assumed as initial input parameters, and subsequently refined through targeted sensitivity-based calibration to improve accuracy (Section 6.1). In general, fracture energies need to be determined for each specific material type through experimental tests, namely compaction tension tests—to characterize intralaminar tensile and compression fracture energies (longitudinal and transverse)— and double-cantilever-beam (DCB) tests to determine interlaminar fracture energies.

Table 2. Fracture energies for longitudinal and transverse directions.

Property	Type-A, B and C
Longitudinal Tensile Fracture Energy (LT-FE) (MPa.mm)	100
Longitudinal Compressive Fracture Energy (LC-FE) (MPa.mm)	600
Transverse Tensile Fracture Energy (TT-FE) (MPa.mm)	5
Transverse Compressive Fracture Energy (TC-FE) (MPa.mm)	20

A small damage stabilization factor value of 1×10^{-4} is also provided to stabilize the damage progression. The explicit solver successfully simulates the analysis of all materials and configurations, as reported and discussed in the following subsections.

4.2. "Type-A" Simulations

For Type-A tests, load–displacement curves were obtained for each considered configuration and compared against the experimental results in Figure 9. Generally, the responses matched closely in the elastic region, and the peak loads were accurately predicted for all end distances.

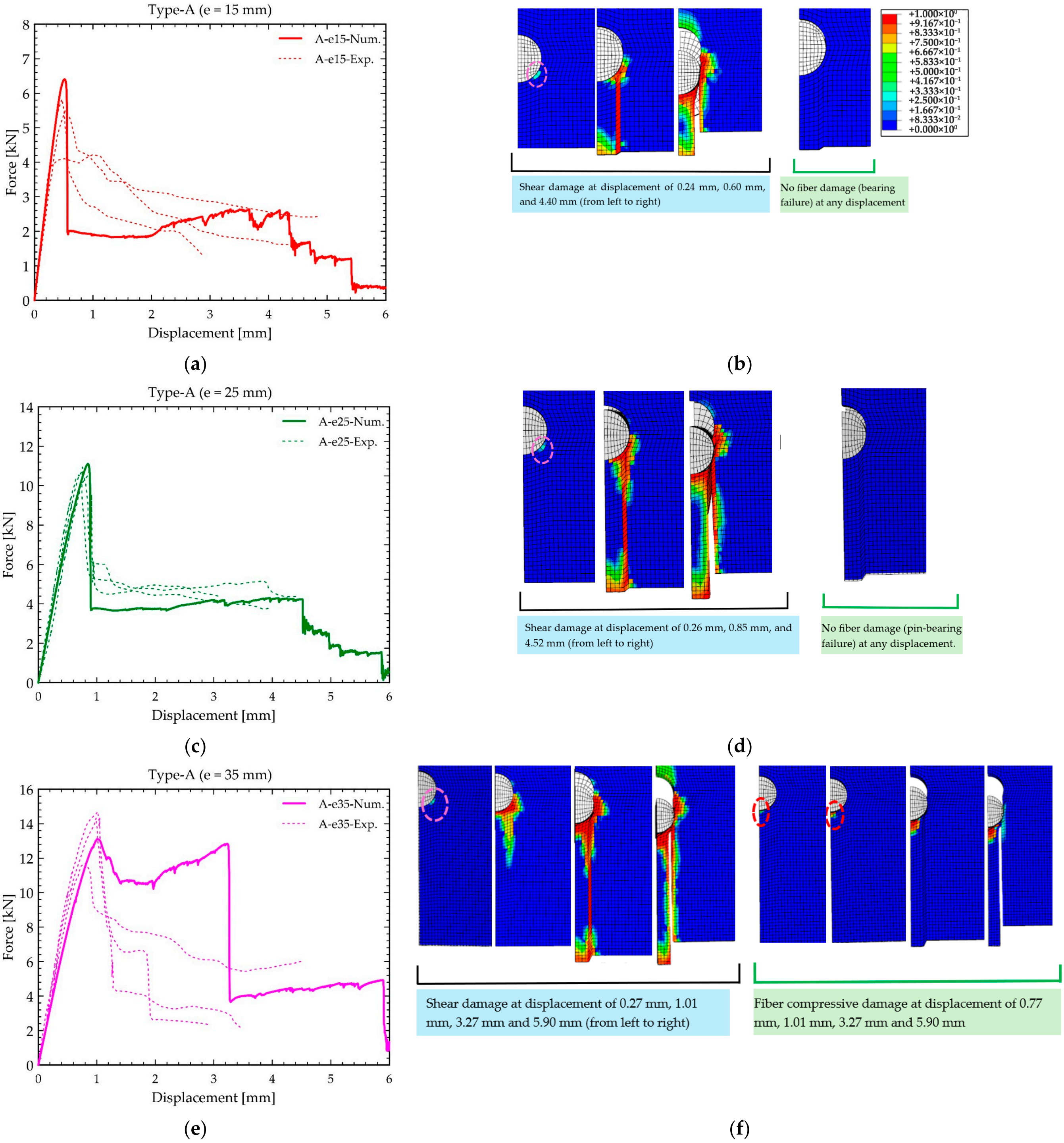

Shear damage at displacement of 0.24 mm, 0.60 mm, and 4.40 mm (from left to right)

No fiber damage (bearing failure) at any displacement

(**a**) (**b**)

Shear damage at displacement of 0.26 mm, 0.85 mm, and 4.52 mm (from left to right)

No fiber damage (pin-bearing failure) at any displacement.

(**c**) (**d**)

Shear damage at displacement of 0.27 mm, 1.01 mm, 3.27 mm and 5.90 mm (from left to right)

Fiber compressive damage at displacement of 0.77 mm, 1.01 mm, 3.27 mm and 5.90 mm

(**e**) (**f**)

Figure 9. *Cont.*

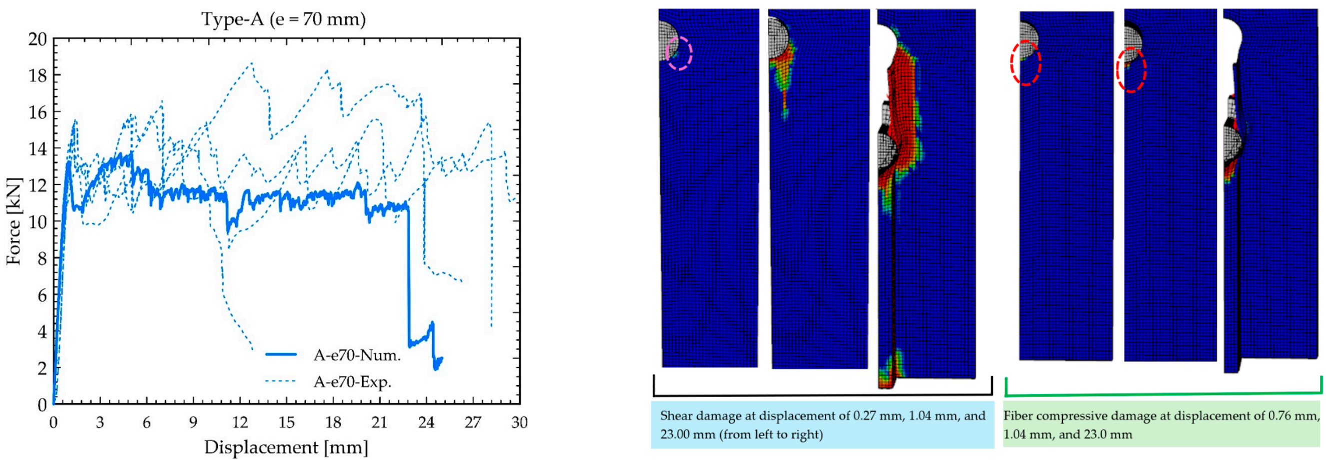

(**g**) (**h**)

Figure 9. Numerical vs. experimental results for "Type-A" tests: (**a**,**c**,**e**,**g**) load vs. displacement graphs, and (**b**,**d**,**f**,**h**) damage at various displacements, for end distances of (**a**,**b**) 15 mm, (**c**,**d**) 25 mm, (**e**,**f**) 35 mm and (**g**,**h**) 70 mm.

The sudden load drop, indicative of shear-out failure onset, was well captured for the configurations with e = 15 mm (Figure 9a) and e = 25 mm (Figure 9c), as evidenced also from the comparison between the numerical and experimental failure patterns (Figure 9b and d, respectively). The shear damage in some elements around the lateral sides of the hole on the compressed edge started at around 3.40 kN at a displacement of 0.24 mm in the model with e = 15 mm, as well as at 4.1 kN and a displacement of 0.26 mm in the model with e = 25 mm, and then progressed in the longitudinal, loading direction in the elements along the end distance on the shear-out plane (Figure 9b,d). The first sudden reduction in resistance occurred at a displacement of 0.6 mm and a peak load of 6.40 kN (for e = 15 mm), or 0.85 mm (for e = 25 mm), when all the elements along the end distance of the shear-out planes became damaged and the shear damage variable index became 1. As the shear-out failure occurred, the capacity curve progressed with residual load, until a second reduction occurred at a displacement of 4.40 mm (e = 15 mm) or 4.52 mm (e = 25 mm), when the separation of the shear-out plane from the main plate occurred, as the elements along the plane attained full damage. Figure 9b,d also show that no fibre compression damage occurred throughout the analysis. Therefore, no bearing failure was activated in the model with e = 15 mm and e = 25 mm.

On the opposite side, in the case where e = 70 mm, the bearing failure was correctly simulated, as can be seen both from the post-peak pseudo-ductile phase of the capacity curves (Figure 9g) and from the concentration of the compressive damage in the fibres around the bolt (Figure 9h), which reflects the experimental damage pattern. The activation of shear damage in elements around the hole started at a displacement of 0.27 mm and at a load around 4.30 kN, as was the case for the model with e = 25 mm, and then progressed as illustrated in Figure 9h. Within the elastic region, this shear damage decreased the stiffness of the capacity curve. The longitudinal compression damage in elements around the compressed edge of the plate near the bolt started at around 11.20 kN and became full damage at a load of 13.25 kN (displacement 1.04 mm), where the pin-bearing failure activated. The pin-bearing failure progressed with even more elements becoming damaged under longitudinal compression. In the mean time, the shear damage in elements along the shear-out plane also progressed, almost reaching one-fourth of the end distance at the point of pin-bearing failure (Figure 9h). Moreover, when all elements along the end distance on the shear plane became fully damaged, the final shear-out failure activated at a large displacement (23.00 mm), where the resistance suddenly dropped from 10.58 kN to 3.1 kN.

In the case where e = 35 mm (Figure 9e,f), shear damage also started at a displacement of 0.27 mm in elements around the plate hole, which started to decrease the stiffness of the curve within the elastic limit. Fibre compression damage started later at a displacement of 0.77 mm (load is 11.21 kN similar to e = 70 mm). At the peak load, pin-bearing failure first became activated in the numerical model at a displacement of 1.01 mm, and was then followed by shear-out failure at a displacement of 3.25 mm. Actually, the post-peak behaviour that resulted was overestimated in the portion before the shear-out failure occurred. However, as can be seen from the capacity curve, the forces corresponding to the activation of the two failure modes were very close. This confirms that the 35 mm end distance is approximately the threshold at which the transition between brittle shear-out and ductile pin-bearing failure occurs in Type-A materials (as also evidenced in Section 3.1). Further sensitivity analysis is required to carefully calibrate the elastic moduli and strength parameters to directly attain shear-out failure without the activation of pin-bearing. However, the purpose here is to show the results obtained using the average mechanical parameters available in the literature, as achieved via the standard characterization tests carried out on the pultruded material. The final shear damage and fibre compression damage at a displacement of 5.90 mm are also shown in Figure 9f, where the separation of some portion from the main plate occurs.

No convergence issues emerged in all the simulated configurations, even when some portion of the main plate became separated from it due to full damage to the elements. Figure 10 contains a plot of the percentage ratio of kinetic energy (KE) to internal energy (IE), as the applied displacement increased, in the four numerical simulations. It emerges that the kinetic energy remained below 1% of the internal energy throughout the analysis, ensuring that the system behaved in a quasi-static manner during the entire simulation, and thus proving the reliability of the stress and strain results of the analyses.

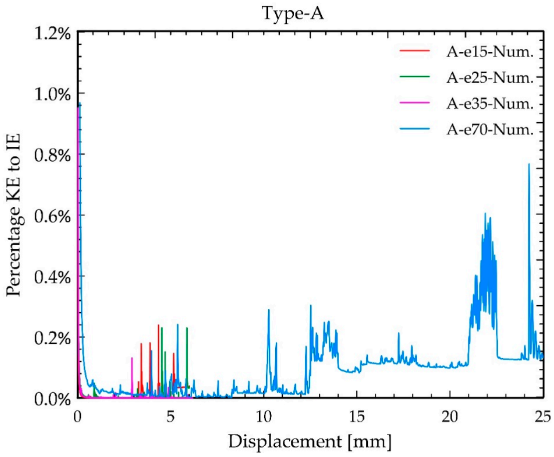

Figure 10. Percentage of kinetic energy (KE) to internal energy (IE) for the "Type-A" models.

4.3. *"Type-B" Simulations*

The resulting load–displacement curve of "Type-B" configurations (Figure 11a,c) demonstrated quite good agreement with the corresponding experimental data. However, the peak load was somewhat overestimated in the case of the joint with d = 16 mm, while in the case of the joint with d = 12 mm, the peak load was accurately estimated but the behaviour after pin-bearing was underestimated. The final shear-out failure observed after the large displacement was consistent with the experimental results of the joints. The final failure patterns for both configurations are presented in Figure 11b,d, showing a strong correlation with the experimentally observed damage modes. In Figure 11b, the initiation and evolution of shear and compression damage are shown for the case with d = 16 mm. The shear damage around the hole started at around 6 kN, at a displacement of 0.058 mm, and progressed within the elements along the end distance on the shear-out plane. The shear damage within the elastic limit reduced the stiffness of the capacity curve. Pin-bearing failure occurred at around 0.75 mm (29.50 kN), where the elements around the plate hole on the compressed end reached full compression damage. Then, the shear damage also progressed along the end distance and covered more than half of the end distance. Complete shear-out failure occurred at around 3.20 mm, where all the elements along the end distance on the shear plane became fully damaged under shear. The final shear-out damage and fibre compression damage at a displacement of 5.95 mm are also shown in Figure 11b. Similarly, the initiation and progression of shear and compression damage are also shown for the case with d = 12 mm (Figure 11d). In this case, the shear damage started at a displacement of 0.04 mm and load of 3.2 kN, affecting the stiffness of the capacity curve. Pin-bearing failure occurred at a relative displacement of 0.68 mm (18.51 kN); shear-out failure occurred at a displacement of 2.95 mm, where the resistance dropped from 19 kN to 8 kN. The final shear-out damage and fibre compression damage that occurred at a relative displacement of 4.79 mm are also shown in Figure 11d.

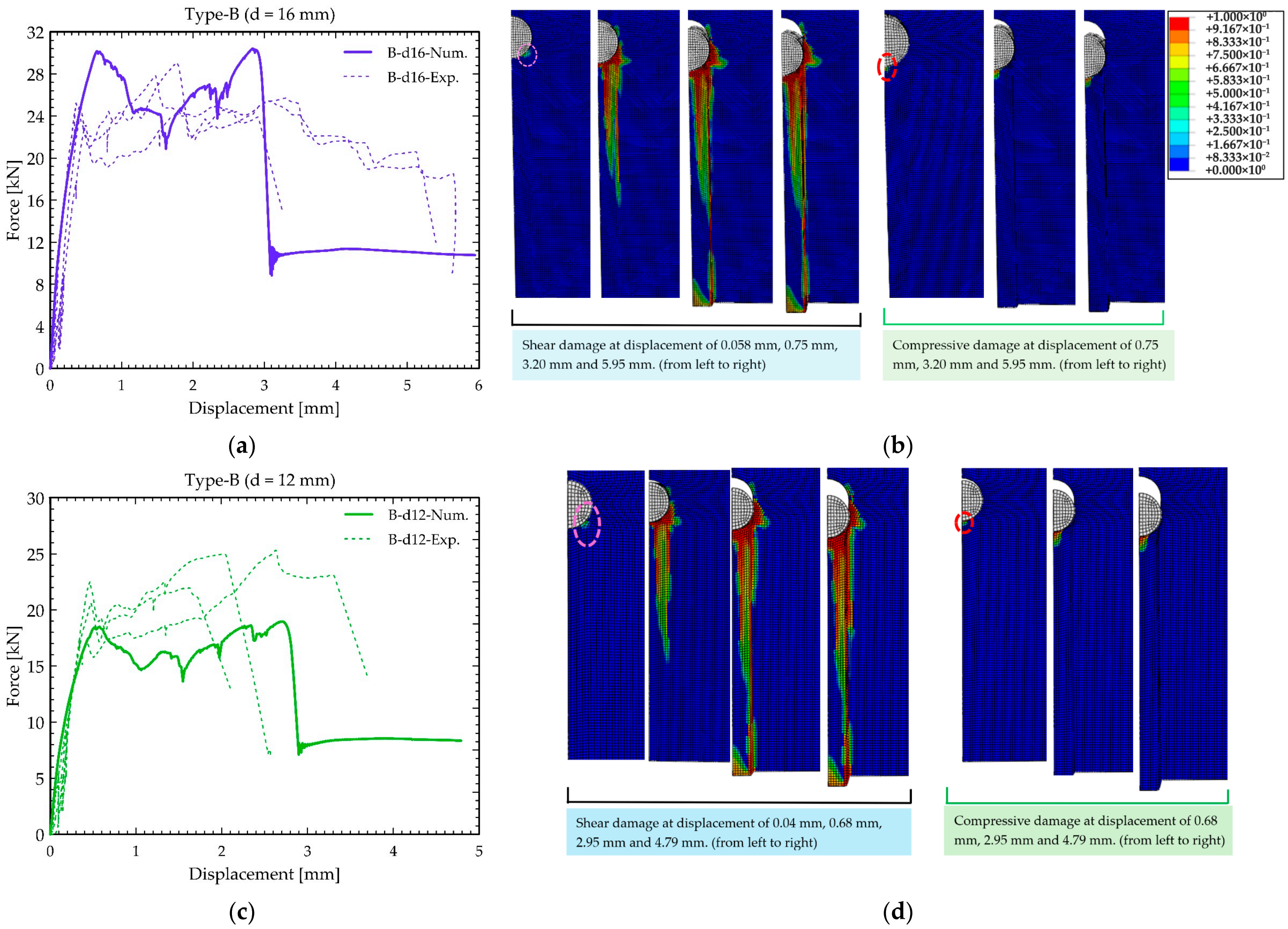

(**a**) (**b**)

(**c**) (**d**)

Figure 11. Numerical vs. experimental results for "Type-B" tests: (**a**,**c**) load vs. displacement graphs, and (**b**,**d**) damage at the end of the test, for (**a**,**b**) M16 and (**c**,**d**) M12 pins.

No convergence issues were encountered during the simulation, enabling analysis under large-displacement conditions. The percentage of kinetic energy (IE) to internal energy (IE) was also less than 1%, which further confirms the quasi-static behaviour of the model (Figure 12).

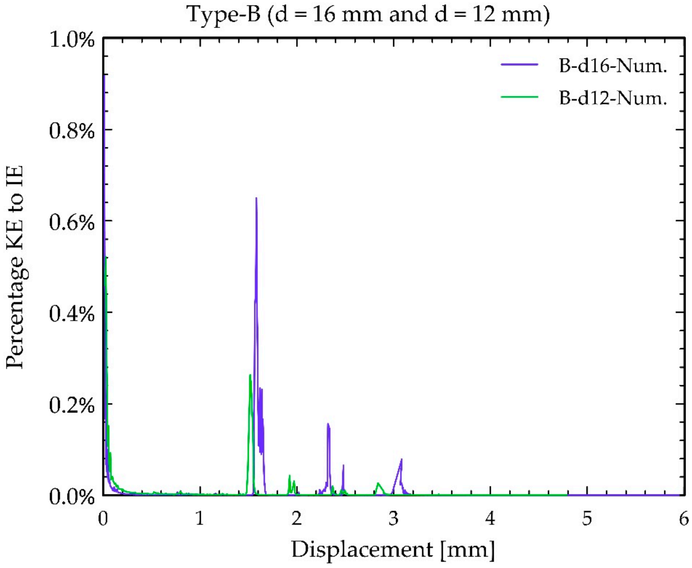

Figure 12. Percentage of kinetic energy (KE) to internal energy (IE) for the "Type-B" models.

4.4. *"Type-C" Simulations*

The Type-C configuration was modelled and simulated, generally applying the features outlined in Section 2, but the full asymmetric double connection is required to be explicitly modelled. In the model, the inner steel plate was fixed, while gradually increasing displacement was applied to the inner GFRP plate. The two outer GFRP plates, along with the portion of the inner GFRP plate away from the bolt, were assigned purely elastic properties, which are detailed in Table 1, since these regions remained elastic throughout the test. Only the area of the inner GFRP plate surrounding the bolt, where plasticization and failure occurred experimentally, was modelled with nonlinear properties from Tables 1 and 2. To account for the effects of slip at the clamping heads, linear springs were introduced at the far ends of the inner plates. Moreover, to account for the hole clearance, a gap of 1 mm was introduced in the bolt–plate contacts. To simplify the representation of the friction between the plates, due to the small bolt torque, rigid-plastic springs acting in the loading direction were also added to connect adjacent plates.

Following this setup, the model was simulated to obtain the load–displacement response, which was then compared with that in the experimental results, as shown in Figure 13a. The initial trend was captured accurately by the model, and the peak load also showed good agreement with the experimental results. However, the resulting post-peak behaviour was governed by sudden shear-out failure. The damage pattern indicated that bearing failure (compression damage) initiated simultaneously with the onset of shear-out failure, as shown in Figure 13b. Furthermore, shear-out was predominant in the numerical simulation, while in the experiment, it declined linearly. In this case, shear damage started at a relative higher displacement of 2.60 mm (9.1 kN) in contrast to the case for the Type-A and Type-B materials due to the effect of the bolt torque (Figure 13b). Shear-out failure occurred at a displacement of 6.10 mm, where the resistance dropped from 38.42 kN to 16.70 kN. Fibre compression in the elements around the hole on the compressed side of plate started at a displacement of 3.86 mm and at a resistance of 20.70 kN. The elements around the hole were almost completely damaged under fibre compression at a displacement of 5.94 mm (38.33 kN). However, at the same time, at a displacement of 6.10 mm, sudden shear-out failure also occurred. The final shear-out damage and fibre compression damage at a displacement of 7.33 mm are shown in Figure 13b, which shows that some portion of the main plate was separated from it along the end distance.

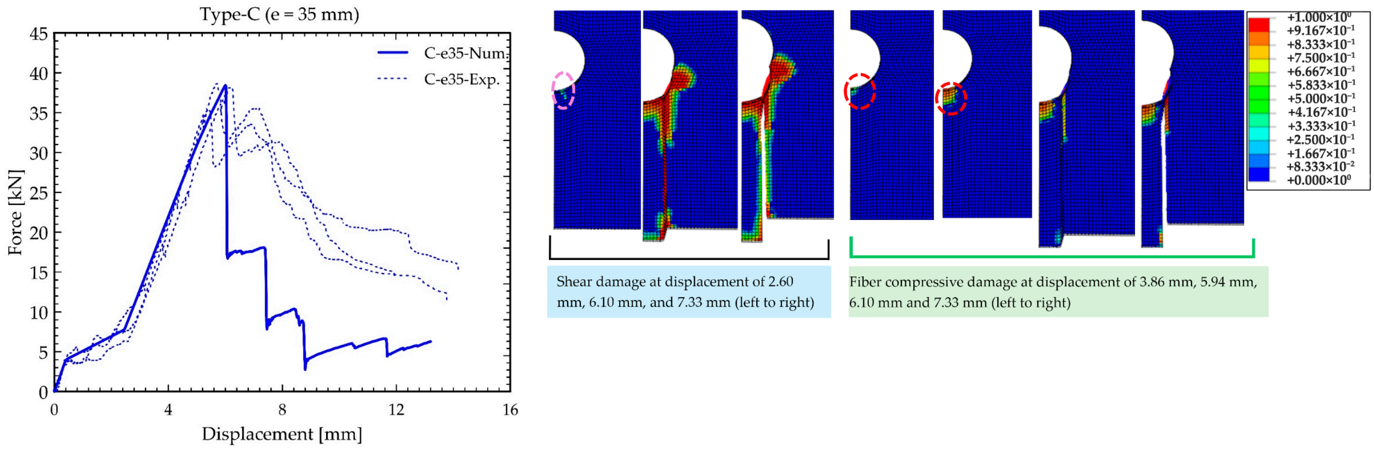

Shear damage at displacement of 2.60 mm, 6.10 mm, and 7.33 mm (left to right)

Fiber compressive damage at displacement of 3.86 mm, 5.94 mm, 6.10 mm and 7.33 mm (left to right)

(**a**) (**b**)

Figure 13. Numerical vs. experimental results for "Type-C" tests: (**a**) load vs. displacement graphs, and (**b**) damage at 6.40 mm.

No convergence issues were encountered during the simulation, enabling analysis under large-displacement conditions. The percentage of kinetic energy (IE) to internal energy (IE) was also less than 1%, which further confirms the quasi-static behaviour of the model (Figure 14).

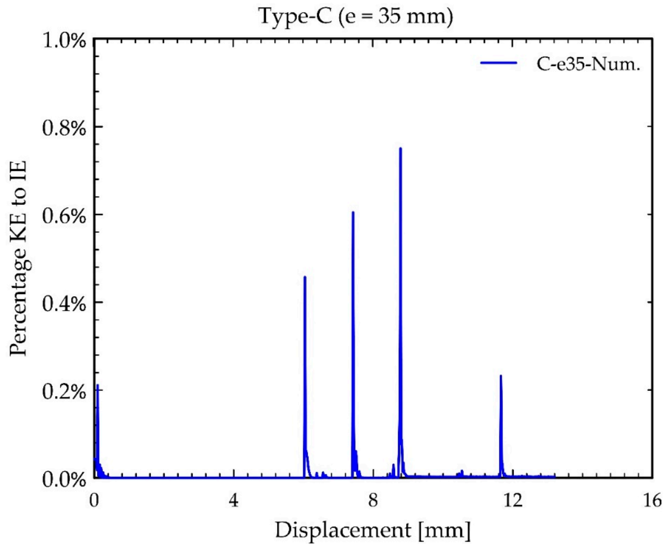

Figure 14. Percentage of kinetic energy (KE) to internal energy (IE) for the "Type-C" model.

5. Sensitivity Analysis for Computational Efficiency

Prior to setting the definitive model features described above, a sensitivity analysis was performed to reduce computational costs while maintaining solution accuracy. Type-A tests were considered as an example. Key parameters such as mesh size and mass scaling (MS) were investigated.

5.1. Implicit Solver

An implicit solver with a general static procedure was used to perform the same simulations with the same parameters as those used for the explicit solver, as this required less computational time. The resulting load–displacement curves were compared with those of the explicit solver, as shown in Figure 15.

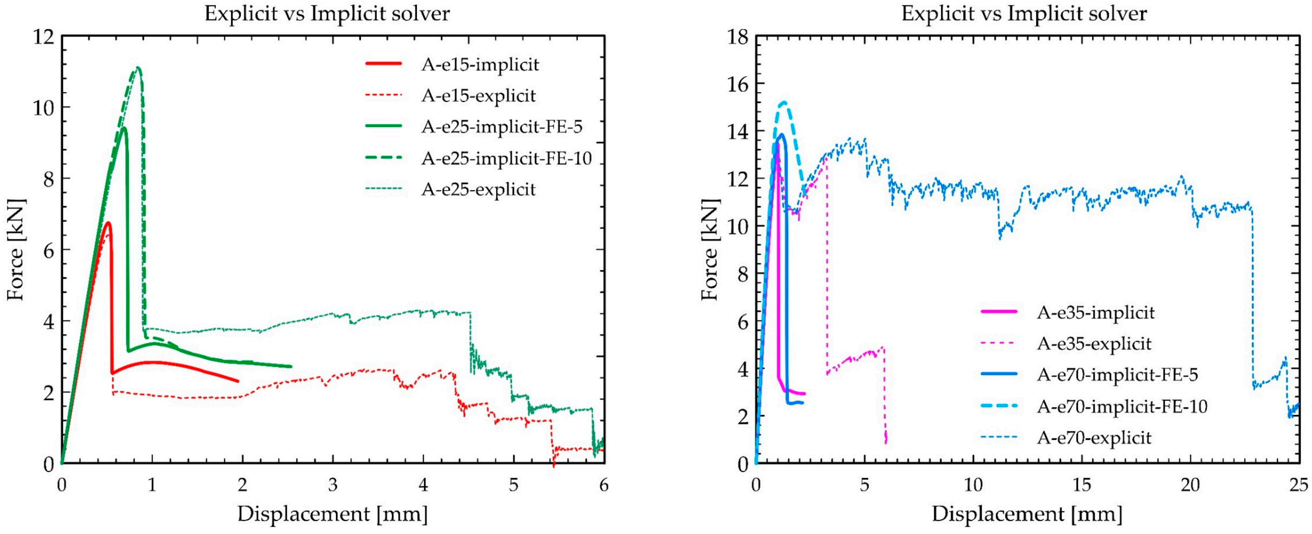

(**a**) (**b**)

Figure 15. Implicit vs. explicit solver numerical results for "Type-A" tests for end distances of (**a**) 15 and 25 mm, and (**b**) 35 and 70 mm.

The results evidence that the implicit solver properly captured the initial loading stage, along with the shear-out failure mode in the configurations with smaller end distances (e = 15, 25, 35 mm). However, the peak load in the configuration with e = 25 mm was underestimated, and required an increase in the original transverse tensile fracture energy (from 5 to 10 MPa·mm). Moreover, larger differences in the post-peak residual load estimations emerged, and the simulations struggled with convergence issues in the nonlinear range after a certain displacement stage (2–2.5 mm). The differences that arose are attributed to the different solver algorithms used.

In the case of the e = 70 mm configuration, the original parameters incorrectly led to shear-out failure; an increase in the original transverse tensile fracture energy (i.e., 10 MPa·mm) would have been required to achieve pin-bearing-dominated failure. However, the main drawbacks occurred in the case analysis performed later, when the implicit solver encountered significant convergence difficulties after damage initiation and peak load attainment, leading to the premature termination of the analysis (at about 2–2.5 mm). The implicit solver in ABAQUS is efficient but, due to convergence issues, was not suitable to simulate the pin-bearing failure of GFRP-bolted connections with the considered material model. Therefore, even though requiring more computational time, ABAQUS/Explicit turned out to be more versatile for simulating the different failure modes of a composite connection.

5.2. Mass Scaling Strategy

Mass scaling (MS) was applied to decrease the analysis duration by introducing artificial mass, which increased the stable time increment and thus reduces the total number of increments required. This technique was implemented with caution, as any mishandling may have affected the reliability and accuracy of the results. According to the ABAQUS documentation, the maximum stable time increment is given by the following:

$$\Delta t_{STABLE} \leq \frac{L_C}{c_d} \tag{1}$$

where Δt_{STABLE} is the stable time increment, L_C is the smallest size in the mesh and c_d is the dilatational wave speed of the material, which can be calculated as follows:

$$c_d = \sqrt{\frac{E}{\rho}} \tag{2}$$

Here, E is the young modulus of the material and ρ is the density of the material. In the case of GFRP, which is an orthotropic material, the stable time increment was determined for both directions, and the smallest stable time increment was selected to remain on the safer and more conservative side. The stable time increments for the longitudinal and transverse direction were 2×10^{-7} and 5.5×10^{-7}, respectively. It is noted that the above expressions are most accurate for materials with a low or zero Poisson's ratio; hence, larger increments were also tested as part of the sensitivity analysis.

For the joint with a 25 mm end distance, the stable time increment without mass scaling was approximately 4.2×10^{-8}, leading to a single simulation runtime of about 24.82 h on an eight-core CPU machine. To address this, mass scaling was applied in separate simulations with target increments of 1×10^{-7}, 2×10^{-7}, 3×10^{-7}, 5×10^{-7}, 1×10^{-6}, and 5×10^{-6}, while keeping all other parameters constant. The total computation time for each case is shown in Table 3. The corresponding structural responses (capacity curves) were plotted to evaluate the impact of mass scaling in Figure 16a. The results show that up to target increment of 1×10^{-6}, they are in high agreement with the non-scaling results. The results for the target increment of 5×10^{-6} showed higher deviations at displacements of 1.2 mm and 4.4 mm, while for the rest of the increments, they matched very well with the results with no mass scaling. The percentages of kinetic energy to internal energy vs. the displacement were also plotted for all mass scaling scenarios (Figure 16b). The percentage ratio was very small up to 0.4% for all target displacements up to 1×10^{-6}; however, it was very large for a target increment of 5×10^{-6}. Furthermore, the results show that, in the latter case, there was a higher percentage ratio of KE to IE at 1.2 mm and 4.4 mm; the results deviate to a large extent from the results for no mass scaling. The mass scaling sensitivity analysis revealed that the optimum duration for the analysis can be 2.58 h for an end distance of 25 mm, with reliable accuracy.

Table 3. Analysis duration with mass scaling for Type-A model with end distance of 25 mm and 70 mm.

Mass Scaling (MS) (Target Increment)	**Computational Time (Hours) for Model (e = 25 mm)**	**Computational Time (Hours) for Model (e = 70 mm)**
No-MS	24.82	41.65
1×10^{-7}	11.66	17.78
2×10^{-7}	5.65	8.88
3×10^{-7}	3.88	6.11
5×10^{-7}	2.58	3.61
1×10^{-6}	1.11	1.94
5×10^{-6}	0.30	0.81

Similarly, mass scaling sensitivity analysis was carried out for a joint with an end distance of 70 mm (Figure 16c) and target increment times of 1×10^{-7}, 2×10^{-7}, 3×10^{-7}, 5×10^{-7}, 1×10^{-6} and 5×10^{-6}. The analysis without mass scaling required a huge computational time of 41.65 h on a machine with eight-core CPUs. The duration time significantly reduced to 3.61 h, with a target increment of 5×10^{-7}. The dynamic effects started from a target increment of 1×10^{-6}, where the percentage of kinetic energy to internal energy became higher than 1%, as shown in Figure 16d. Also in this case, the target increment of 5×10^{-7} provided the optimum duration of 3.61 h for the analysis, with reliable accuracy.

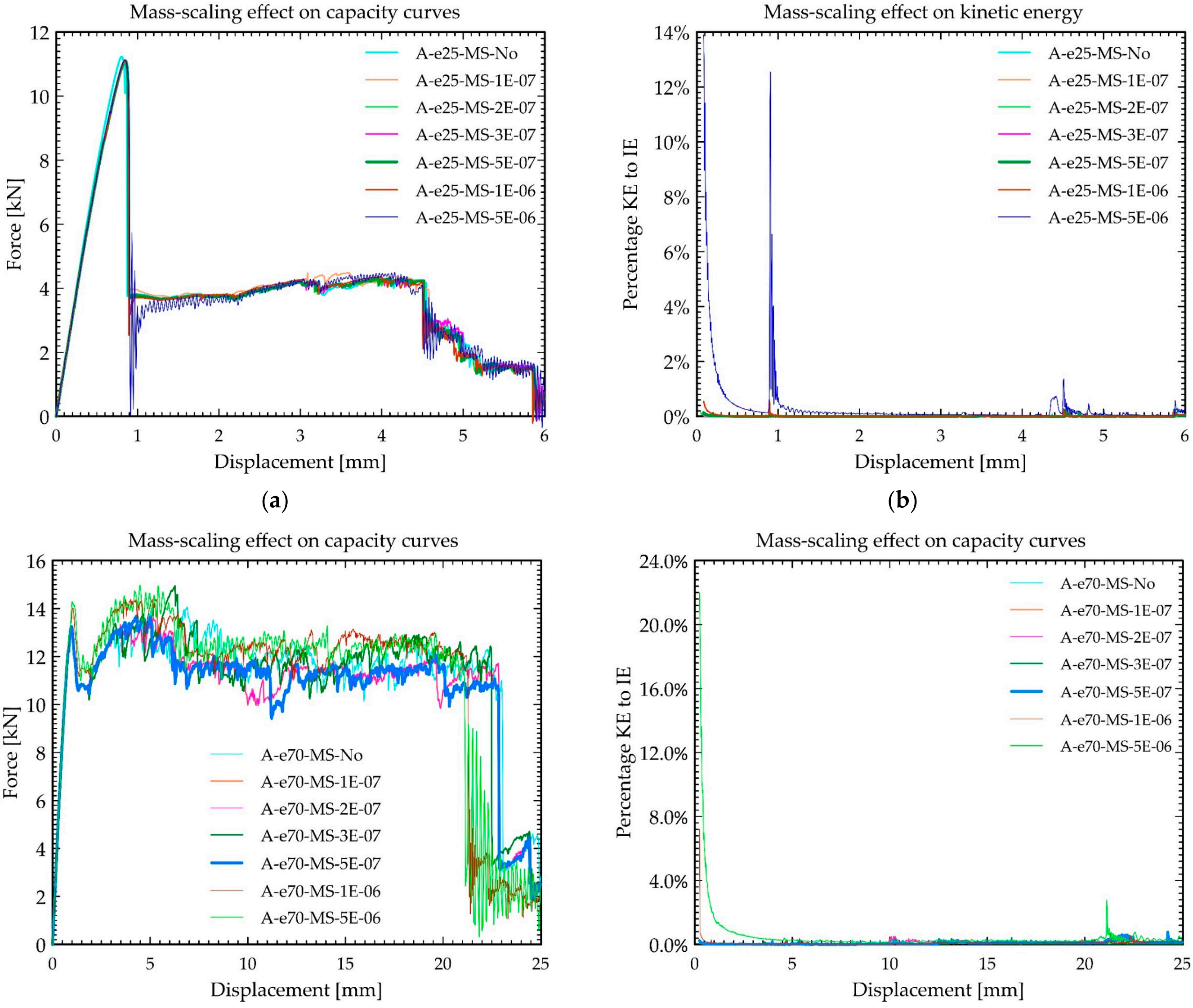

(**a**) (**b**)

(**c**) (**d**)

Figure 16. Effect of mass scaling increments: (**a**,**c**) load vs. displacement graph and (**b**,**d**) percentage of kinetic energy (KE) to internal energy (IE) for "Type-A" models with (**a**,**b**) 25 mm and (**c**,**d**) 70 mm end distances.

5.3. Mesh Sensitivity Analysis

A mesh sensitivity analysis was performed to evaluate the influence of mesh refinement on the accuracy, reliability, and computational cost of the nonlinear analysis of the GFRP inelastic section only. The two end distances of 25 mm and 70 mm were investigated.

A series of mesh sizes were examined, ranging from very fine to very coarse configurations, while keeping all other parameters constant. The reference mesh was a fine mesh measuring $0.7 \times 0.7 \times 1$ mm^3, containing 6040 elements. The finest resolution of $0.5 \times 0.5 \times 1$ mm^3, resulting in 11,888 elements, was considered. Subsequently, lower-resolution meshes were tested, including $0.8 \times 0.8 \times 1$ mm^3 (4532 elements), $1.0 \times 1.0 \times 1.0$ mm^3 (2856 elements) and $1.5 \times 1.5 \times 1.0$ mm^3 (1236 elements). The respective mass scaling target increment factors, which were different for each mesh size, were calculated from Equation (1).

The capacity curves for the *e* = 25 mm configuration (Figure 17a) show that for all meshes, the elastic region was the same, followed by very similar peak loads. However, different residual loads were observed in all cases after the first drop. The residual load was the highest with the finest mesh containing 11,888 elements, while it was the smallest for the coarse and very coarse meshes, with 4532, 2656 and 1236 elements. The fine mesh (6080 elements) had an intermediate residual load value. Furthermore, the second reduction was observed only for the finest mesh with 11,888, 6080, and 4532 elements, leading to a second reduction with finest mesh size early on. On the other hand, in the case of the coarse and very coarse mesh sizes, the capacity curves showed an increasing trend instead of a second reduction. This led to the conclusion that the desired behaviour starts with a coarse mesh size with 4532 elements, while a 6080-element mesh size, which shows an intermediate residual load and a definite second reduction, is an optimize mesh size to consider with regards to computation time and accuracy.

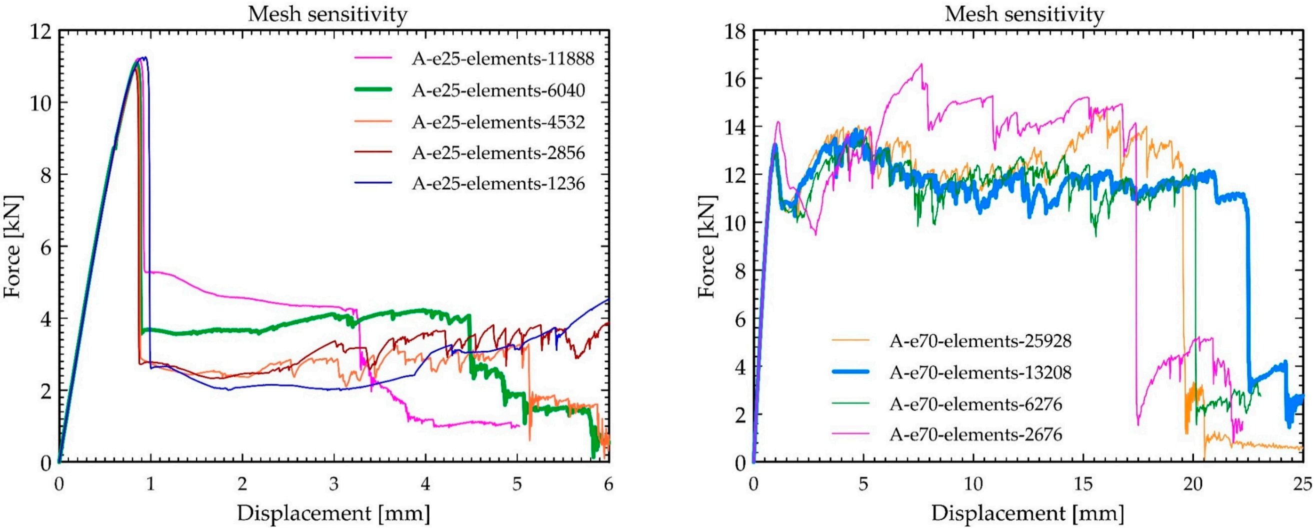

(**a**) (**b**)

Figure 17. Load vs. displacement graph for model with (**a**) 25 mm and (**b**) 70 mm end distances, with varying mesh sizes in inelastic part of GFRP plate.

The capacity curves for the *e* = 70 mm configuration are presented in Figure 17b. The very coarse mesh exhibited a higher peak load, with results that were significantly skewed, showing underestimations after the peak load and overestimations beyond a displacement of 5 mm. Moreover, the very coarse mesh also accelerated the final shear-out failure. The coarser mesh produced a peak load comparable to that of the fine and very fine meshes, though with slightly more scattered results. The fine and very fine meshes displayed nearly identical behaviour, maintaining consistency up to a displacement of 11 mm. The final shear-out failure occurred at slightly different displacements, with the finest mesh size accelerating this shear-out failure compared to the fine mesh. Overall, when comparing the behaviours, the mesh with 13,208 elements provided stable and consistent results closely matching those of the very fine mesh. Consequently, this mesh size was selected for the simulations, to ensure a balance between computational efficiency and accuracy.

6. Mechanical Parametric Study

6.1. Fracture Energy Parameter Sensitivity

To understand the behaviour of the Hashin damage criterion in individual failure modes, a sensitivity analysis was first carried out using a $10 \times 10 \times 10$ mm^3 cube model. This preliminary study aimed to evaluate how different failure modes are triggered independently, considering that in a bolted joint, all failure modes may be activated even under uniaxial tensile or compressive loading. The cube was modelled using continuum shell elements and subjected first to pure longitudinal tensile loading, and then longitudinal compressive loading followed by transverse tensile and compressive loading. A mesh size of 0.7 × 0.7 × 1 mm^3 was used to capture the damage's initiation and progression accurately. The aim of the simulation was to observe the crack/crush initiation point and the post-peak behaviour based on varying values of longitudinal tensile and compression fracture energy (FE), ranging from 50 MPa·mm to 600 MPa·mm. For the transverse direction, the range selected was from 1 MPa·mm (indicating brittle behaviour) to 100 MPa·mm (suggesting ductile response), as the strength and elastic modulus in this direction are significantly smaller than those in the main longitudinal direction.

The obtained stress–strain curves (Figure 18a,b) revealed a typical pattern: an initial linear elastic region, followed by damage initiation at peak load, and then a gradual or steep linear strength reduction depending on the fracture energy. Lower fracture energy led to a sharper post-peak drop, indicating brittle failure, whereas higher fracture energy resulted in a gentler slope, representing more ductile behaviour.

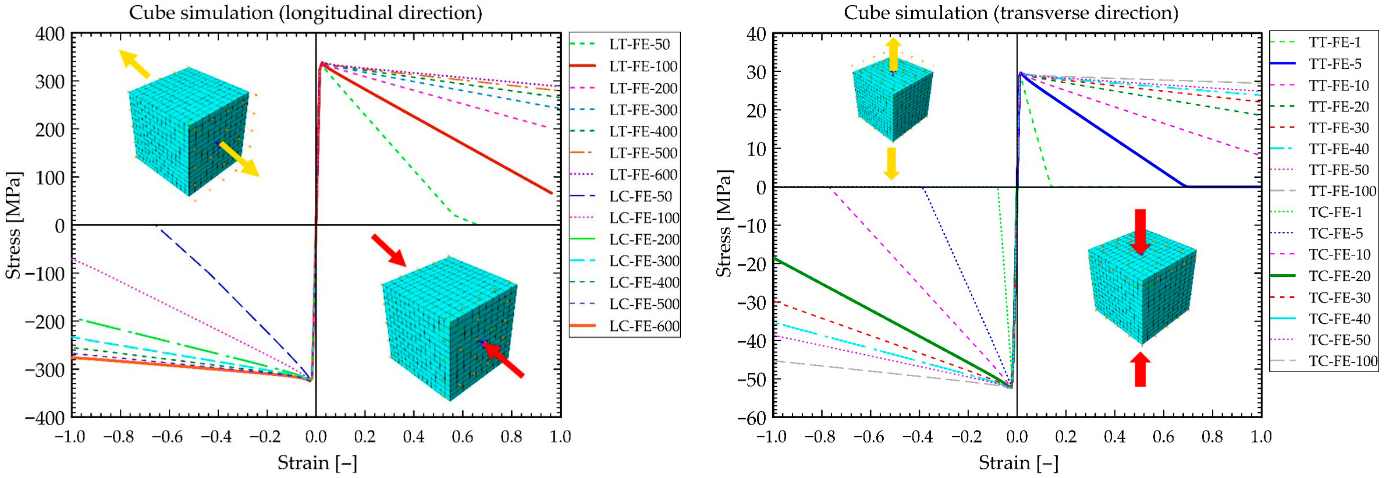

(**a**) (**b**)

Figure 18. Load–displacement graph for cube model under (**a**) pure longitudinal tensile and compressive loading; (**b**) pure transverse tensile and compressive loading.

Experimental evidence and the literature indicate that pultruded GFRP profiles exhibit brittle behaviour under longitudinal tension, with many researchers using a fracture energy value around 100 MPa·mm, which aligns with a steep post-peak decline [43]. It was also observed that under pure longitudinal tensile loading, fracture energies in other directions had negligible influence; the damage's evolution was governed solely by the longitudinal tensile fracture energy. On the other hand, the compressive behaviour of pultruded GFRP is typically less brittle than that under in tension, and thus a relatively higher fracture energy value of 600 MPa·mm was selected for the bolted joint simulations.

The sensitivity analysis for fracture energies was also carried out using the Type-A model with e = 25 mm and 70 mm. For the model with e = 25 mm, the first sensitivity study was performed on the transverse tensile fracture energy, varying it from the original 5 MPa·mm to 1 MPa·mm, 10 MPa·mm, and 20 MPa·mm. The load–displacement graphs (Figure 19a) revealed that, as the transverse tensile fracture energy increased, both the peak load and the residual strength increased. A notable difference was observed between the peaks corresponding to 5 MPa·mm and 1 MPa·mm; with 1 MPa·mm, the second reduction occurred at a much earlier stage (1.21 mm). When increasing the fracture energy beyond 5 MPa·mm to 10 MPa·mm and 20 MPa·mm, the increase in peak load was smaller compared to the difference observed at 1 MPa·mm. In all cases except 1 MPa·mm, the second reduction occurred at approximately the same displacement of 4.52 mm, as all elements along the end distance on the shear plane became fully damaged. From this analysis, it is concluded that the transverse tensile fracture energy significantly affects the peak load, the residual strength, and the behaviour after the residual load.

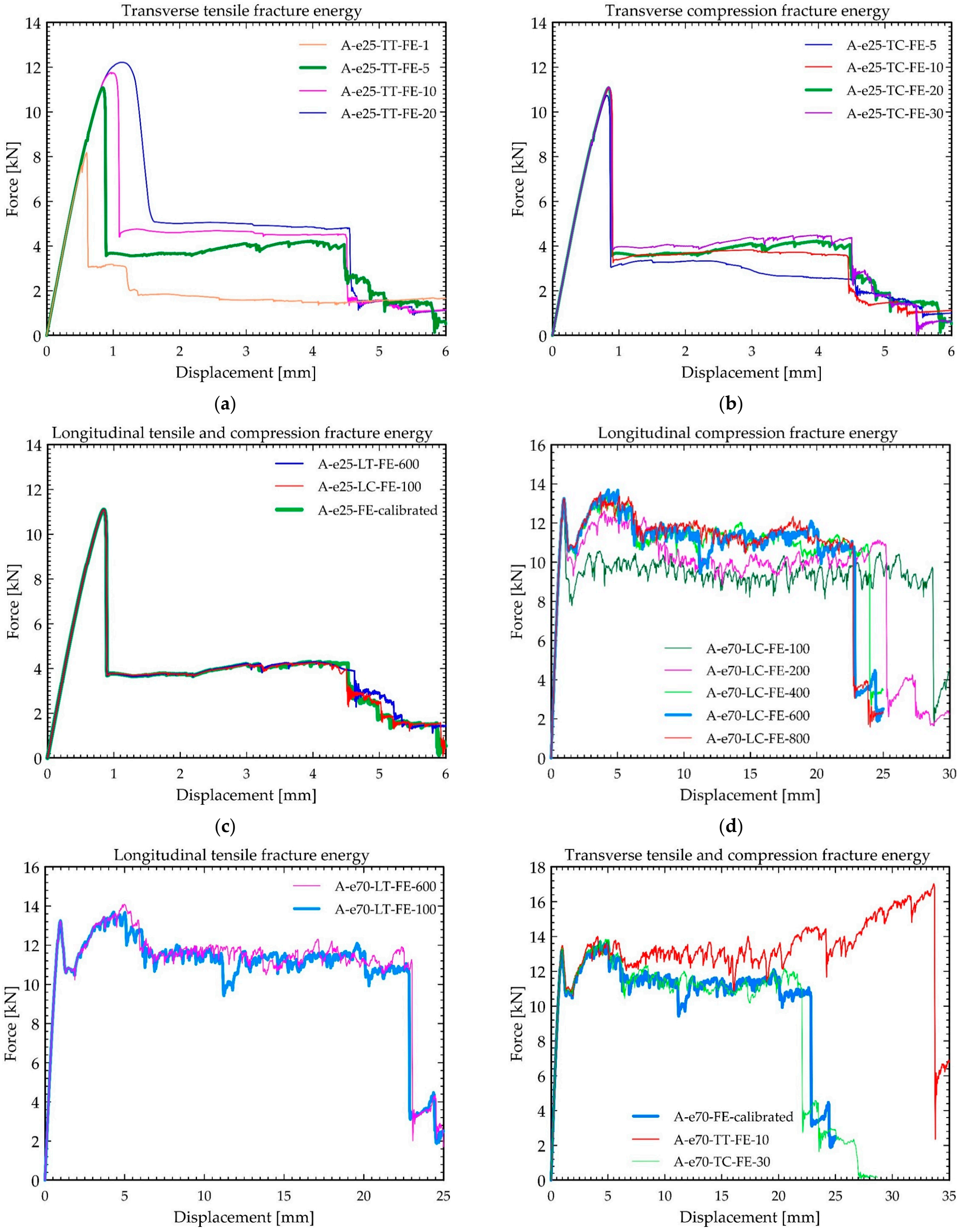

(**a**) (**b**)

(**c**) (**d**)

(**e**) (**f**)

Figure 19. Load–displacement curves from sensitivity analysis of fracture energies (F.E): (**a**–**c**) for a 25 mm end distance: (**a**) transverse tensile F.E, (**b**) transverse compression F.E, and (**c**) longitudinal tensile and compression fracture energies; (**d**–**f**) for a 70 mm end distance: (**d**) longitudinal compression F.E, (**e**) longitudinal tensile F.E, and (**f**) transverse tensile and compression fracture energies.

Similarly, sensitivity analysis was performed for the transverse compression fracture energy, and the resulting capacity curves were plotted (Figure 19b). The results showed no effect on the peak load; however, the residual load after the peak was slightly influenced. The post-peak behaviour was more noticeably influenced when the fracture energy was raised from 5 MPa·mm to 10 MPa·mm, while it was less prominent when it was further increased from 20 MPa·mm to 30 MPa·mm. The second reductions after the residual behaviour consistently occurred at a displacement of approximately 4.52 mm.

Furthermore, the longitudinal tensile fracture energy was increased from 100 MPa·mm to 600 MPa·mm, and the longitudinal compression fracture energy was decreased from 600 MPa·mm to 100 MPa·mm. As expected, the resulting capacity curves (Figure 19c), compared with the standard fracture energy curve, indicated no significant effect on behaviour. Only a slight increase was observed after the second drop in residual strength in the case of a 600 MPa·mm tensile fracture energy. Overall, it can be concluded that longitudinal tensile and compression fracture energies have minimal impact in joints dominated by shear-out failure.

For the model with a 70 mm end distance, for which the dominant failure mode was bearing failure, the first sensitivity study was conducted by varying the longitudinal compression fracture energy from 100 MPa·mm to 800 MPa·mm. The curves (Figure 19d) show that the first peak load remained unaffected by changes in longitudinal compression fracture energy. However, the first drop after the peak was more pronounced for 100 MPa·mm and 200 MPa·mm than for 400 MPa·mm, 600 MPa·mm, and 800 MPa·mm; in the latter cases, it became stabilized. Additionally, the second peak after the first drop was more prominent and comparable for the 400/600/800 MPa·mm cases, slightly lower for the 200 MPa·mm condition and notably reduced for the 100 MPa·mm condition. The displacement related to the final shear-out failure, which occurred after large deformations, tended to increase as the fracture energy decreased (22.9 mm for 800 MPa·mm, 23.0 mm for 600 MPa·mm, 24.0 mm for 400 MPa·mm, 25.5 mm for 200 MPa·mm, and 29 mm for 100 MPa·mm).

Similarly, the longitudinal tensile fracture energy was increased from 100 MPa·mm to 600 MPa·mm, and the resulting capacity curves were plotted (Figure 19e). This increase had almost no effect on the overall behaviour, although it helped stabilize the small, local load reduction at around 11 mm. This stabilization is attributed to the limited longitudinal tensile damage occurring in a few elements around the hole, which was better controlled by higher tensile fracture energy. Nonetheless, it did not impact the bearing failure mode of the joint. However, it is reasonable to assume that the composite in tension had relatively brittle behaviour, as has already been discussed.

Additionally, the transverse tensile fracture energies, which increased from 5 MPa·mm to 10 MPa·mm, and transverse compression fracture energies, which increased from 20 MPa·mm to 30 MPa·mm, were investigated (Figure 19f). The increase in the transverse tensile fracture energy did not influence the peak load or the subsequent load reduction, which was associated with bearing failure, but led to an increased post-peak load response after reaching about 6 mm, as well as an evident delay in the onset of the final shear-out failure (at 33.6 mm). However, increasing the transverse compressive fracture energy exhibited a negligible impact on both the peak load and the overall load–displacement behaviour just slightly before the final shear-out failure.

In conclusion, the analysis clearly indicates that for the joint with shear-out failure as the dominant mode, the transverse tensile fracture energy played the most significant role. It directly influenced the peak load, the residual strength, and the overall post-residual behaviour of the connection. In contrast, variations in the other fracture energies—namely longitudinal tensile, longitudinal compression, and transverse compression—exhibited negligible effects on the global response under this configuration. Differently, for the joint where bearing failure governed the response, the behaviour was primarily affected by the longitudinal compression fracture energy. Changes in this parameter notably alter the post-peak behaviour and the progression towards the final shear-out failure. In addition, the transverse tensile fracture energy showed an appreciable influence at large displacements, also affecting the final stage of shear-out failure. On the other hand, the longitudinal tensile and transverse compression fracture energies had a minimal impact on the overall structural behaviour.

6.2. Strength Parameter Sensitivity

The variation in the main strength parameters was investigated for both shear-out and bearing failure-dominated connections, using the Type-A model with *e* = 25 mm and 70 mm, respectively.

At first, the shear strength was varied from the standard 35 MPa to 25 MPa and 45 MPa. Predictably, the results showed that shear strength has a significant impact on the peak load for the model with *e* = 25 mm (Figure 20a). Specifically, the peak load increased with increasing shear strength. The post-peak residual resistance, however, was similar in all cases, as it was primarily influenced by the transverse tensile fracture energy (as previously demonstrated in Section 6.1), which remained the same across the three models with different shear strengths. Notably, for the model with a shear strength of 25 MPa, the second drop occurred earlier (3 mm) than for the 35 MPa and 45 MPa models (4.5 mm). Similarly, for the model with an end distance of e = 70 mm, the shear strength had a significant influence on the peak load (Figure 20b). An increase in shear strength not only raises the peak load but also delays the onset of final shear-out failure, resulting in an overall increasing trend for this behaviour in the load–displacement response.

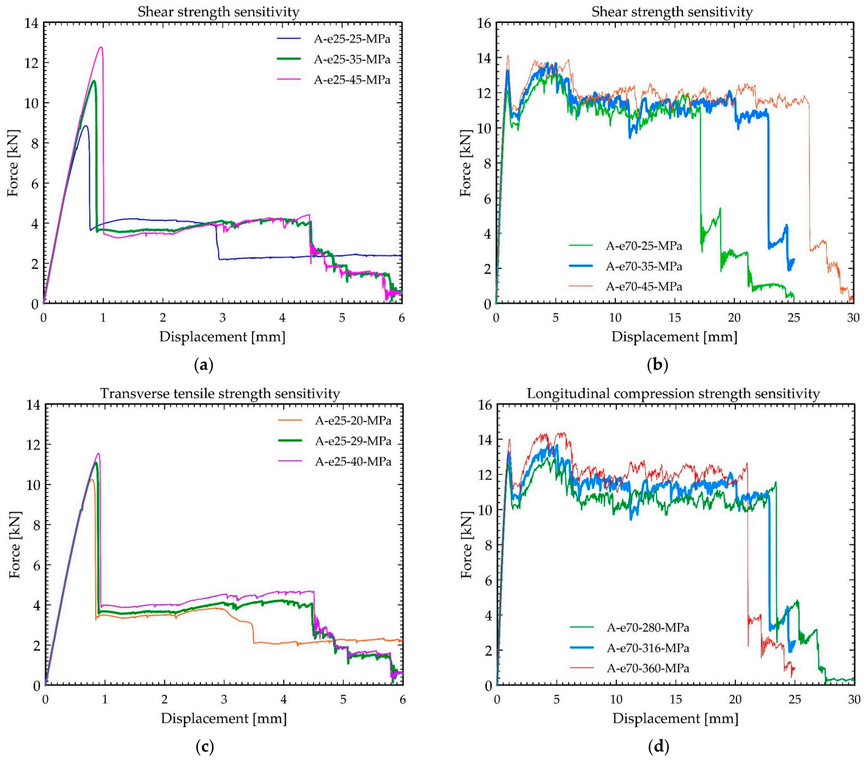

(**a**) (**b**)

(**c**) (**d**)

Figure 20. Load–displacement curves from parametric strength values: (**a**) for shear strength in model with 25 mm end distance, (**b**) shear strength in model with 70 mm end distance; (**c**) transverse tensile strength in model with 25 mm end distance: (**d**) longitudinal compressive strength in model with 70 mm end distance.

The effect of transverse tensile strength was also investigated by varying it from the standard 29 MPa to 20 MPa and 40 MPa for model with e = 25 mm. The results (Figure 20c) indicate that the peak load was slightly affected, with a similarly minor impact on the post-peak behaviour, until about 3 mm. However, for the model with the lower transverse tensile strength, the second drop occurred earlier, at a displacement of around 3 mm.

To investigate the influence of the longitudinal compression strength in the model with e = 70 mm, the strength value varied from the standard 316 MPa to 280 MPa and 340 MPa. The results (Figure 20d) show that with higher compression strength, the peak load slightly increases, the post-peak behaviour exhibits an upward trend, and the final shear-out failure occurs earlier, consistent with the observations made for variations in longitudinal compression fracture energy.

7. Conclusions

In this study, comprehensive and detailed numerical simulations were carried out to investigate the behaviour of GFRP double-lap bolted joints using ABAQUS/Explicit. Three different GFRP materials with varying geometric configurations for double-lap joints were modelled. The inbuilt Hashin failure criteria were employed for damage initiation and progression, with damage evolution governed by calibrated fracture energies in both the longitudinal and transverse directions. The following key conclusions were drawn:

- Capturing Different Failure Modes in A Simulation: The explicit solver simulations effectively captured distinct failure modes, including shear-out and pin-bearing failures. The numerical results showed good agreement with experimental observations across most configurations. However, for joints representing a transition between bearing and shear-out dominated failures, further calibration of the elastic moduli, strengths and fracture energies is recommended to improve the predictive accuracy. Furthermore, the shear-out failure in the numerical simulations appeared more abrupt compared to the slightly less steep strength reduction observed in experiments, due to the current inherent limitation of purely brittle intralaminar failure formulations in the ABAQUS material model. Further refinement should include linear or exponential declination. However, shear-out failure is undesirable from the structural design point of view, since this implies a sudden failure of the connection. Conversely, the goal is to design connections governed by a pin-bearing mechanism, which—as clearly proven experimentally—exhibits pseudo-ductile behaviour. This aspect is particularly important in multi-bolt connections, as it enables effective load redistribution. Shear-out failure that appears slightly more brittle than that observed experimentally can be considered, in this sense, a conservative assumption. Additionally, it is important to note that the fracture energy values employed in this study were calibrated and adopted from the existing literature, without direct experimental validation specific to the materials under investigation. Similarly, certain strength parameters were assumed based on typical values reported in the literature, rather than being determined through dedicated experimental characterization. These aspects introduce inherent limitations to the predictive accuracy of the models, particularly when extending the findings to different geometries or loading scenarios.
- Explicit/Implicit Solver Performance: The explicit solver successfully simulated all models with different end distances and material types, reliably capturing damage initiation and progression without any convergence issues. On the other hand, the implicit solver consistently struggled with post-damage initiation, particularly failing to model bearing failures beyond the onset of damage. The implicit solver also struggled in the case of shear-out failure for larger deformations. This highlights

the explicit solver’s outstanding capability for simulating progressive damage in GFRP-bolted joints.

- Mass Scaling and Mesh Sensitivity: Mass scaling techniques were successfully applied, reducing the computational time from 24–42 h to approximately 2–6 h without compromising accurateness of the results. Mesh sensitivity analysis was also performed to optimize element counts, ensuring a balance between computational efficiency and numerical precision.
- Fracture Energy Sensitivity: Systematic sensitivity analysis was conducted to investigate the role of different fracture energies on the peak load, residual load after the peak load and post-peak failure behaviour. Transverse tensile fracture energy had the most pronounced effect on shear-out failures, directly influencing the peak load, the residual load after the first peak, and the final post-residual load drop. Increasing this parameter also delayed the onset of the final shear-out failure. The other longitudinal tensile and compression fracture energies and transverse compression fracture energies have minimal impact on the overall behaviour of the shear-out failure. Longitudinal compression fracture energy primarily affects the pin-bearing response, while transverse tensile fracture energy has no effect on the peak load and overall behaviour. However, it only delays the final shear-out failure when increased. The other fracture energies have no impact on the behaviour of pin-bearing failure.
- Parametric Study On Strength Parameters: Parametric analyses were performed considering the tensile, compression and shear strength. The shear-out-dominated failure was most sensitive to in-plane shear strength and transverse tensile strength: an increase in these parameters elevated the peak load and enhanced the post-peak response. In configurations dominated by pin-bearing failure, both shear strength and longitudinal compressive strength significantly influenced the bearing behaviour. Increasing these strengths raised the peak load and improved the overall load–displacement response, and the shear strength delayed the final shear-out failure.
- Limitation of Numerical Models: The developed numerical models are well suited for accurately simulating double-lap bolted joints, where out-of-plane stresses and deformations are minimal. That is why continuum shell elements, which neglect out-of-plane stresses and reduce the computational time, were employed; in this specific case, this simplification does not affect the accuracy of the results. However, for single-lap joints, where significant out-of-plane bending and associated stresses occur, the current modelling approach could become inadequate, and the continuum shell elements may no longer be appropriate. Accurately capturing these three-dimensional stress states would require the use of solid 3D elements in combination with user-defined material subroutines (UMAT or VUMAT) in ABAQUS, since the built-in Hashin failure criteria in ABAQUS apply only to shell and continuum shell elements. This underscores the necessity of using advanced modelling techniques to accurately predict the complex failure mechanisms in single-lap GFRP bolted joints. However, employing UMAT or VUMAT subroutines will substantially increase both the computational cost and complexity of numerical simulations.
- Future Work: The present model has so far been established and validated mainly for in-plane loading conditions and specific connection configurations. Its applicability to different geometries and loading scenarios therefore remains to be evaluated. Thus, now that the material models have been validated and the influence of the key parameters has been established through detailed parametric studies, this research will be further extended to investigate multiple bolted connections, as well as the strengthening of single- and multi-bolted joints, e.g., by using externally bonded fibre-reinforced sheets. For this purpose, the modelling assumptions and simplifications of

the model are deemed sufficiently accurate to support reliable simulation. Nevertheless, ongoing study is also directed toward extending the model to transversal and inclined loading conditions. Alongside the numerical simulations, experimental tests are currently being carried out to refine the model on the basis on the specific PFRP material, through comparison with the experimental results of single-bolt tests, and to validate the developed model, through comparison with the experimental results of multi-bolt connections.

Author Contributions: Conceptualization and methodology, A.R., I.B. and N.G.; investigation, A.R.; data curation, A.R. and I.B.; writing—original draft preparation, A.R. and I.B.; writing—review and editing, A.R., I.B. and N.G.; visualization, A.R.; supervision, project administration, and funding acquisition, N.G. All authors have read and agreed to the published version of the manuscript.

Funding: This research received no external funding.

Data Availability Statement: The data is contained within the article.

Acknowledgments: The authors gratefully acknowledge the support of the Italian Ministry of University and Research (MUR) for partly funding this research. They also express appreciation and gratitude for the partial financial support provided by Fibrenet Industry, Pavia di Udine, Italy.

Conflicts of Interest: The authors declare no conflicts of interest.

Abbreviations

The following abbreviations are used in this manuscript:

PFRP	Pultruded-Fibre-Reinforced Polymer
CSM	Chopped Stranded Mat
GFRP	Glass-Fibre-Reinforced Polymer
FE	Finite Element
VUMAT	Vectorized User Material
UMAT	User Material
SC8R	Continuum Shell Elements with 8 Nodes and Reduced Integration
C3D8R	Continuum 3D Solid Elements with Reduced Integration
FE	Fracture Energy
LT-FE	Longitudinal Tensile Fracture Energy
LC-FE	Longitudinal Compressive Fracture Energy
TT-FE	Transverse Tensile Fracture Energy
TC-FE	Transverse Compressive Fracture Energy
KE	Kinetic Energy
IE	Internal Energy
MS	Mass Scaling

References

1. Bank, L.C. *Composites for Construction*; Wiley: Hoboken, NJ, USA, 2006; ISBN 9780471681267.
2. Hollaway, L.C. A Review of the Present and Future Utilisation of FRP Composites in the Civil Infrastructure with Reference to Their Important In-Service Properties. *Constr. Build. Mater.* **2010**, *24*, 2419–2445. [CrossRef]
3. Balsamo, A.; Coppola, L.; Zaffaroni, P. FRP in Construction: Applications, Advantages, Barriers and Perspectives. In Proceedings of the International Workshop, Composites in Construction: A Reality, Capri, Italy, 20–21 July 2001; American Society of Civil Engineers: Reston, VA, USA, 2012; pp. 58–64.
4. Qureshi, J. A Review of Fibre Reinforced Polymer Structures. *Fibers* **2022**, *10*, 27. [CrossRef]
5. Karbhari, V.M.; Zhao, L. Use of Composites for 21st Century Civil Infrastructure. *Comput. Methods Appl. Mech. Eng.* **2000**, *185*, 433–454. [CrossRef]
6. Correia, J.R.; Keller, T.; Knippers, J.; Mottram, J.T.; Paulotto, C.; Sena-Cruz, J.; Ascione, L. *Design of Fibre-Polymer Composite Structures: Commentary to European Technical Specification CEN/TS 19101: 2022*; CRC Press: Boca Raton, FL, USA, 2025; ISBN 1040151876.

7. Girão Coelho, A.M.; Mottram, J.T. A Review of the Behaviour and Analysis of Bolted Connections and Joints in Pultruded Fibre Reinforced Polymers. *Mater. Des.* **2015**, *74*. [CrossRef]
8. Naser, M.Z.; Hawileh, R.A.; Abdalla, J.A. Fiber-Reinforced Polymer Composites in Strengthening Reinforced Concrete Structures: A Critical Review. *Eng. Struct.* **2019**, *198*, 109542. [CrossRef]
9. Siddika, A.; Al Mamun, M.A.; Ferdous, W.; Alyousef, R. Performances, Challenges and Opportunities in Strengthening Reinforced Concrete Structures by Using FRPs—A State-of-the-Art Review. *Eng. Fail. Anal.* **2020**, *111*, 104480. [CrossRef]
10. Kouris, L.A.S.; Triantafillou, T.C. State-of-the-Art on Strengthening of Masonry Structures with Textile Reinforced Mortar (TRM). *Constr. Build. Mater.* **2018**, *188*, 1221–1233. [CrossRef]
11. Babatunde, S.A. Review of Strengthening Techniques for Masonry Using Fiber Reinforced Polymers. *Compos. Struct.* **2017**, *161*, 246–255. [CrossRef]
12. Boem, I. Masonry Elements Strengthened with TRM: A Review of Experimental, Design and Numerical Methods. *Buildings* **2022**, *12*, 1307. [CrossRef]
13. Hammad, M.; Bahrami, A.; Khokhar, S.A.; Khushnood, R.A. A State-of-the-Art Review on Structural Strengthening Techniques with FRPs: Effectiveness, Shortcomings, and Future Research Directions. *Materials* **2024**, *17*, 1408. [CrossRef] [PubMed]
14. Rosner, C.N.; Rizkalla, S.H. Bolted Connections for Fiber-Reinforced Composite Structural Members: Experimental Program. *J. Mater. Civ. Eng.* **1995**, *7*, 223–231. [CrossRef]
15. El-Sisi, A.; Hassanin, A.; Alsharari, F.; Galustanian, N.; Salim, H. Failure Behavior of Composite Bolted Joints: Review. *CivilEng* **2022**, *3*, 1061–1076. [CrossRef]
16. Feroldi, F.; Russo, S. Structural Behavior of All-FRP Beam-Column Plate-Bolted Joints. *J. Compos. Constr.* **2016**, *20*, 04016004. [CrossRef]
17. Martins, D.; Gonilha, J.; Correia, J.R.; Silvestre, N. Exterior Beam-to-Column Bolted Connections between GFRP I-Shaped Pultruded Profiles Using Stainless Steel Cleats. Part 1: Experimental Study. *Thin-Walled Struct.* **2021**, *163*, 107719. [CrossRef]
18. Turvey, G.J. Single-Bolt Tension Joint Tests on Pultruded GRP Plate—Effects of Tension Direction Relative to Pultrusion Direction. *Compos. Struct.* **1998**, *42*, 341–351. [CrossRef]
19. Abd-El-Naby, S.F.M.; Hollaway, L. The Experimental Behaviour of Bolted Joints in Pultruded Glass/Polyester Material. Part 1: Single-Bolt Joints. *Composites* **1993**, *24*, 531–538. [CrossRef]
20. Cooper, C.; Turvey, G.J. Effects of Joint Geometry and Bolt Torque on the Structural Performance of Single Bolt Tension Joints in Pultruded GRP Sheet Material. *Compos. Struct.* **1995**, *32*, 217–226. [CrossRef]
21. Tajeuna, T.A.; Légeron, F.; Langlois, S.; Labossière, P.; Demers, M. Effect of Geometric Parameters on the Behavior of Bolted GFRP Pultruded Plates. *J. Compos. Mater.* **2016**, *50*, 3731–3749. [CrossRef]
22. Gattesco, N.; Boem, I. A Numerical Study on Multiple Bolted Connections through Glass Pultruded Members. In Proceedings of the Fifteenth International Conference on Civil, Structural and Environmental Engineering Computing, Prague, Czech Republic, 1–4 September 2015; Bell & Bain Ltd.: Glasgow, UK, 2015.
23. *E. 13706 CEN*; Reinforced Plastics Composites—Specifications for Pultruded Profiles. Part 1: Designation; Part 2: Methods of Test and General Requirements; Part 3: Specific Requirements. CEN: Brussels, Belgium, 2002.
24. Clarke, J.L. *EUROCOMP Design Code and Handbook: Structural Design of Polymer Composites*; E & FN Spon: London, UK, 1996.
25. *CNR-DT "205/2007"*; Guide for the Design and Construction of Structures Made of FRP Pultruded Elements. Advisory Committee on Technical Recommendations for Constructions, Italian National Research Council: Rome, Italy, 2007.
26. Hashin, Z. Failure Criteria for Unidirectional Fiber Composites. *J. Appl. Mech.* **1980**, *47*, 329–334. [CrossRef]
27. Puck, A.; Schürmann, H. Failure Analysis of FRP Laminates by Means of Physically Based Phenomenological Models. In *Failure Criteria in Fibre-Reinforced-Polymer Composites*; Elsevier: Amsterdam, The Netherlands, 2004; pp. 832–876.
28. Pinho, S.T.; Darvizeh, R.; Robinson, P.; Schuecker, C.; Camanho, P.P. Material and Structural Response of Polymer-Matrix Fibre-Reinforced Composites. *J. Compos. Mater.* **2012**, *46*, 2313–2341. [CrossRef]
29. Börgesson, L. Abaqus. In *Developments in Geotechnical Engineering*; Elsevier: Amsterdam, The Netherlands, 1996; Volume 79, pp. 565–570. ISBN 0165-1250.
30. Feo, L.; Marra, G.; Mosallam, A.S. Stress Analysis of Multi-Bolted Joints for FRP Pultruded Composite Structures. *Compos. Struct.* **2012**, *94*, 3769–3780. [CrossRef]
31. Turvey, G.J.; Wang, P. An FE Analysis of the Stresses in Pultruded GRP Single-Bolt Tension Joints and Their Implications for Joint Design. *Comput. Struct.* **2008**, *86*, 1014–1021. [CrossRef]

32. Zhou, Y.; Yazdani-Nezhad, H.; McCarthy, M.A.; Wan, X.; McCarthy, C. A Study of Intra-Laminar Damage in Double-Lap, Multi-Bolt, Composite Joints with Variable Clearance Using Continuum Damage Mechanics. *Compos. Struct.* **2014**, *116*, 441–452. [CrossRef]
33. Frizzell, R.M.; McCarthy, C.T.; McCarthy, M.A. Predicting the Effects of Geometry on the Behaviour of Fibre Metal Laminate Joints. *Compos. Struct.* **2011**, *93*, 1877–1889. [CrossRef]
34. O'Higgins, R.M.; McCarthy, C.T.; McCarthy, M.A. Effects of Shear-Transverse Coupling and Plasticity in the Formulation of an Elementary Ply Composites Damage Model, Part I: Model Formulation and Validation. *Strain* **2012**, *48*, 49–58. [CrossRef]
35. Egan, B.; McCarthy, M.A.; Frizzell, R.M.; Gray, P.J.; McCarthy, C.T. Modelling Bearing Failure in Countersunk Composite Joints under Quasi-Static Loading Using 3D Explicit Finite Element Analysis. *Compos. Struct.* **2014**, *108*, 963–977. [CrossRef]
36. Okutan, B. The Effects of Geometric Parameters on the Failure Strength for Pin-Loaded Multi-Directional Fiber-Glass Reinforced Epoxy Laminate. *Compos. B Eng.* **2002**, *33*, 567–578. [CrossRef]
37. Tserpes, K.I.; Labeas, G.; Papanikos, P.; Kermanidis, T. Strength Prediction of Bolted Joints in Graphite/Epoxy Composite Laminates. *Compos. B Eng.* **2002**, *33*, 521–529. [CrossRef]
38. Xiao, Y.; Ishikawa, T. Bearing Strength and Failure Behavior of Bolted Composite Joints (Part II: Modeling and Simulation). *Compos. Sci. Technol.* **2005**, *65*, 1032–1043. [CrossRef]
39. Olmedo, Á.; Santiuste, C. On the Prediction of Bolted Single-Lap Composite Joints. *Compos. Struct.* **2012**, *94*, 2110–2117. [CrossRef]
40. Kapidžić, Z.; Nilsson, L.; Ansell, H. Finite Element Modeling of Mechanically Fastened Composite-Aluminum Joints in Aircraft Structures. *Compos. Struct.* **2014**, *109*, 198–210. [CrossRef]
41. Kolks, G.; Tserpes, K.I. Efficient Progressive Damage Modeling of Hybrid Composite/Titanium Bolted Joints. *Compos. Part. A Appl. Sci. Manuf.* **2014**, *56*, 51–63. [CrossRef]
42. Hühne, C.; Zerbst, A.-K.; Kuhlmann, G.; Steenbock, C.; Rolfes, R. Progressive Damage Analysis of Composite Bolted Joints with Liquid Shim Layers Using Constant and Continuous Degradation Models. *Compos. Struct.* **2010**, *92*, 189–200. [CrossRef]
43. Arruda, M.R.T.; Trombini, M.; Pagani, A. Implicit to Explicit Algorithm for ABAQUS Standard User-Subroutine UMAT for a 3D Hashin-Based Orthotropic Damage Model. *Appl. Sci.* **2023**, *13*, 1155. [CrossRef]
44. Egan, B.; McCarthy, C.T.; McCarthy, M.A.; Gray, P.J.; Frizzell, R.M. Modelling a Single-Bolt Countersunk Composite Joint Using Implicit and Explicit Finite Element Analysis. *Comput. Mater. Sci.* **2012**, *64*, 203–208. [CrossRef]
45. Liu, P.; Cheng, X.; Wang, S.; Liu, S.; Cheng, Y. Numerical Analysis of Bearing Failure in Countersunk Composite Joints Using 3D Explicit Simulation Method. *Compos. Struct.* **2016**, *138*, 30–39. [CrossRef]
46. Belardi, V.G.; Fanelli, P.; Vivio, F. Analysis of Multi-Bolt Composite Joints with a User-Defined Finite Element for the Evaluation of Load Distribution and Secondary Bending. *Compos. B Eng.* **2021**, *227*, 109378. [CrossRef]
47. Vangrimde, B.; Boukhili, R. Bearing Stiffness of Glass Fibre-Reinforced Polyester: Influence of Coupon Geometry and Laminate Properties. *Compos. Struct.* **2002**, *58*, 57–73. [CrossRef]
48. *Anon*; Ansys Inc.: Canonsburg, PA, USA, 2006.
49. Bathe, K.J. *ADINA/Standard User's Manual, Version 8.7. 3*; ADINA R&D, Inc.: Watertown, NY, USA, 2011.
50. Du, A.; Liu, Y.; Xin, H.; Zuo, Y. Progressive Damage Analysis of PFRP Double-Lap Bolted Joints Using Explicit Finite Element Method. *Compos. Struct.* **2016**, *152*, 860–869. [CrossRef]
51. Camanho, P.P.; Dávila, C.G. *Mixed-Mode Decohesion Finite Elements for the Simulation of Delamination in Composite Materials*; NASA Langley Research Center: Hampton, VA, USA, 2002.
52. *EN ISO 527-1*; Plastics—Determination of Tensile Properties—Part 1: General Principles. European Committee for Standardization: Brussels, Belgium, 1997.
53. *ASTM D695-02*; Standard Test Method for Compressive Properties of Rigid Plastics. ASTM International: West Conshohocken, PA, USA, 2002.
54. *ISO 14126*; Fibre-Reinforced Plastic Composites—Determination of Compressive Properties in the in-Plane Direction. International Organization for Standardization: Geneva, Switzerland, 1999.
55. *ASTM D 5379/D 5379M*; Standard Test Method for Shear Properties of Composites Materials by the V-Notched Beam Method. ASTM: West Conshohocken, PA, USA, 2005.
56. *BS EN ISO 14130*; Fibre-Reinforced Plastic Composites—Determination of Apparent Interlaminar Shear Strength by Short-Beam Method. British Standards Institution: London, UK, 1998.
57. *ASTM D 2344/D 2344M-00*; Standard Test Method for Short-Beam Strength of Polymer Matrix Composites Materials and Their Laminates. ASTM: West Conshohocken, PA, USA, 2000.
58. Zhang, Y.; Van Paepegem, W.; De Corte, W. An Enhanced Progressive Damage Model for Laminated Fiber-Reinforced Composites Using the 3D Hashin Failure Criterion: A Multi-Level Analysis and Validation. *Materials* **2024**, *17*, 5176. [CrossRef] [PubMed]

59. Mandal, B.; Chakrabarti, A. Simulating Progressive Damage of Notched Composite Laminates with Various Lamination Schemes. *Int. J. Appl. Mech. Eng.* **2017**, *22*, 333–347. [CrossRef]
60. *ISO 527-5, B*; Plastics–Determination of Tensile Properties. British Standard: Bonn, Germany, 1997.
61. Almeida-Fernandes, L.; Silvestre, N.; Correia, J.R.; Arruda, M.R.T. Fracture Toughness-Based Models for Damage Simulation of Pultruded GFRP Materials. *Compos. B Eng.* **2020**, *186*, 107818. [CrossRef]